## Dynamic Musculoskeletal Functional Morphology: Integrating diceCT and XROMM

COURTNEY P. ORSBON , 1\* NICHOLAS J. GIDMARK, AND CALLUM F. ROSS Department of Organismal Biology and Anatomy, The University of Chicago, Chicago, Illinois 60637
Biology Department, Knox College, Galesburg, Illinois 61401

#### ABSTRACT

The tradeoff between force and velocity in skeletal muscle is a fundamental constraint on vertebrate musculoskeletal design (form:function relationships). Understanding how and why different lineages address this biomechanical problem is an important goal of vertebrate musculoskeletal functional morphology. Our ability to answer questions about the different solutions to this tradeoff has been significantly improved by recent advances in techniques for quantifying musculoskeletal morphology and movement. Herein, we have three objectives: (1) review the morphological and physiological parameters that affect muscle function and how these parameters interact; (2) discuss the necessity of integrating morphological and physiological lines of evidence to understand muscle function and the new, high resolution imaging technologies that do so; and (3) present a method that integrates high spatiotemporal resolution motion capture (XROMM, including its corollary fluoromicrometry), high resolution soft tissue imaging (diceCT), and electromyography to study musculoskeletal dynamics in vivo. The method is demonstrated using a case study of in vivo primate hyolingual biomechanics during chewing and swallowing. A sensitivity analysis demonstrates that small deviations in reconstructed hyoid muscle attachment site location introduce an average error of 13.2% to in vivo muscle kinematics. The observed hyoid and muscle kinematics suggest that hyoid elevation is produced by multiple muscles and that fascicle rotation and tendon strain decouple fascicle strain from hyoid movement and whole muscle length. Lastly, we highlight current limitations of these techniques, some of which will likely soon be overcome through methodological improvements, and some of which are inherent. Anat Rec, 301:378-406, 2018. © 2018 Wiley Periodicals, Inc.

Key words: muscle; functional morphology; biomechanics; XROMM; diceCT

Grant sponsors: NIH (NIDCR and NICHD); NSF (MRI and DDRIG); Grant numbers: R01-DE023816 and T32-HD009007 (NIH); DBI-1338066 and BCS-1732175 (NSF)

\*Correspondence to: Courtney P. Orsbon, Department of Organismal Biology and Anatomy, The University of Chicago, Anatomy 407, 1027 East 57<sup>th</sup> Street, Chicago, IL 60637. Tel: (704) 641-7863; Fax: (773) 702-0037 E-mail: orsbon@uchicago.edu

Received 15 June 2017; Revised 5 September 2017; Accepted 11 September 2017.

DOI 10.1002/ar.23714

Published online in Wiley Online Library (wileyonlinelibrary.

#### INTRODUCTION

Musculoskeletal output force, velocity, and displacement play essential roles in organismal performance during a variety of vertebrate behaviors, including feeding and locomotion. Decades of physiological and biomechanical research have revealed a fundamental constraint on musculoskeletal design<sup>1</sup> in vertebrates: the tradeoff between force and velocity due to the basic morphological and physiological properties of vertebrate muscle. The ways in which different lineages deal with this constraint are an important focus of evolutionary biomechanics and neuromechanics.

This article has three objectives. First, we review the morphological and physiological parameters that have been shown to affect muscle function and discuss how these parameters interact. Second, we discuss the necessity of integrating morphological and physiological lines of evidence to understand how the interaction of these parameters affects muscle function. Newly developed, high resolution imaging technologies are advancing muscle functional morphology research through the seamless integration of these lines of evidence. We focus on two of these: diffusible iodine-based contrast enhanced Computed Tomography (diceCT, Gignac et al., 2016) and X-Rav Reconstruction of Moving Morphology (XROMM, Brainerd et al., 2010). Third, we present a method of integrating diceCT and XROMM with electromyography to build a more complete picture of muscle functional morphology and biomechanics.

# PARAMETERS OF PERFORMANCE Morphology

Active muscle force, with its inherent force-velocity tradeoffs, is determined in part by the morphology of muscle fibers (cells) and the way these cells are arranged in whole muscles. Fiber force varies with sarcomere length and shortening velocity, being maximal over an intermediate range of sarcomere lengths and decreasing as fiber shortening velocity increases (Gasser and Hill, 1924; Stevens and Snodgrass, 1932; Ramsey and Street, 1940: Gordon et al., 1966). Muscle architecture (fiber pennation, fiber length, and tendon morphology) determines how these forces are combined and transformed at the whole muscle level (Gans and Bock, 1965; Anapol and Barry, 1996). Specifically, physiological cross-sectional (PCSA) strongly correlates with maximum isometric muscle force (Powell et al., 1984) while fiber length, when normalized by sarcomere length, accurately predicts the range of motion over which the muscle can actively produce isometric force (Felder et al., 2005; Winters et al., 2011). For a given volume of whole skeletal muscle, architecture can vary along a spectrum favoring high velocity on one end and high force on the other (Gans and Bock, 1965; Gans 1982; Gans and de Vree, 1987). Long fibers arranged in parallel to the muscle's line of action place more sarcomeres in series and therefore combine larger displacements and

shortening velocities with lower but more consistent force over a wider range of whole muscle length. In contrast, short fibers arranged at an angle to the line of action (i.e., pennate fibers) place more sarcomeres in parallel and consequently produce higher force over a more limited range of whole muscle length than parallel-fibered muscles.

Muscle attachment site location also impacts forcevelocity tradeoffs. Mechanical advantage—the ratio of the muscle's moment arm from the center of rotation to that of the output and/or reaction forces—determines how the magnitude and direction of muscle force vectors change as bones move into different postures among individual movements, organismal designs, or body sizes (Stern, 1974; Biewener, 1989; Lieber and Fridén, 2000; German et al., 2011). Variation in attachment location relative to the center of rotation, i.e., in-lever length, not only affects output forces but also the magnitude of muscle displacement: longer in-levers require greater changes in muscle length for a given amount of joint rotation (Herring and Herring, 1974; Lieber et al., 1997). Therefore, while joint moment increases with a longer in-lever, such gains come at the cost of a more limited range of joint motion over which the muscle can actively produce force.

These aspects of vertebrate musculoskeletal morphology impact functional system design in a variety of species. In the mammalian feeding system, the fundamental tradeoff between muscle force and displacement manifests as a tradeoff between bite force and gape (Herring and Herring, 1974; Taylor and Vinyard, 2004; Eng et al., 2009; Taylor et al., 2009; Perry et al., 2011; Hartstone-Rose et al., 2012; Hylander, 2013; Taylor and Vinyard, 2013). In the fish feeding system, variation in relative lengths of input and output lever arms maps onto variation in the relative importance of suction feeding (which requires high muscle shortening velocities) and biting (Westneat, 2004). Elegant linkages in the jaws of teleost fish and birds further elaborate on the basic design of skeletal levers to amplify displacement, velocity, and joint moment (Westneat, 1990; Westneat, 2003; Olsen and Westneat, 2016).

While some vertebrates show morphological specialization to optimize force or velocity, tradeoffs can also be negotiated by a medley of more generalized morphologies. To summarize the morphological contributions to muscle function described above, force and velocity can be affected by three different morphological parameters independent of fiber type: 1) the number of sarcomeres in a fiber, 2) muscle architecture, and 3) moment arm length (Lieber and Ward, 2011; Kandel et al., 2012). Because multiple components can interact to produce different amounts of force and velocity, musculoskeletal design is redundant, that is, different forms can function similarly (Lauder, 1990; Lauder, 1995; Wainwright et al., 2005). Therefore, understanding how muscle morphology relates to performance necessarily involves not only analysis of the muscle itself but its moment arm to determine how the two interact to produce output force and displacement. For example, a muscle producing less force inserting further away from an axis of rotation may produce a greater joint moment than a muscle producing more force but inserting closer to the axis of rotation due to the former's larger moment arm, e.g., the human tensor fascia latae versus the more massive

<sup>&</sup>lt;sup>1</sup>Throughout this article, we define musculoskeletal design as the relationship among musculoskeletal morphology, physiology, and biomechanical performance—in short, form:function relationships (Ross et al., 2017).

gluteus maximus (Hoy et al., 1990; Lieber, 2009). In contrast, a muscle with long fibers may have a smaller moment arm than a muscle with a similar line of action but with short fibers, as with the human extensor carpi radialis longus and brevis, respectively (Lieber et al., 1990; Lieber et al., 1997). Long moment arms are not necessarily accompanied by long fibers and vice versa (Maganaris et al., 2006), which limits the functional inferences that can be made from either muscular or skeletal morphology alone.

Additionally, many muscles themselves are redundant because joints frequently have more than one muscle capable of producing movement with a given degree of freedom. In humans, an average of 2.6 muscles controls each degree of freedom (Prilutsky and Zatsiorsky, 2002), and examples of highly redundant movements include jaw elevation, knee extension, and ankle plantarflexion. Mechanical redundancy presents a motor control problem for the brain given the unlimited number of potential kinetic and kinematic solutions (Bernstein, 1967). However, redundancy may also offer a solution to a separate problem presented by the tradeoffs of muscle function: controlling force over a wide range of motion and velocities while decreasing overall muscle mass and its attendant maintenance costs (Lieber and Fridén, 2000). Synergists—muscles capable of producing movement in the same degree of freedom-often vary not only in architecture and moment arm length but also in fiber types (i.e., slow-twitch vs fast-twitch) that can either exacerbate or mitigate functional tradeoffs among the synergists (Spector et al., 1980; Wakeling et al., 2006; Wakeling et al., 2011; Rupert et al., 2015).

While many studies have highlighted how muscle architecture and mechanical advantage relate to performance tradeoffs, functional specialization for force or displacement/velocity is not a universal phenomenon among skeletal muscles. Muscles can produce both higher force and higher excursion and velocity through increased muscle mass (Organ et al., 2009; Taylor and Vinyard, 2009; Terhune et al., 2015), although such increases may be accompanied by a decrease in moment arm length that limits potential gains in output force (Terhune et al., 2015). The presence of a "supermuscle" (sensu Lieber and Fridén, 2000) rather than separate, specialized synergists may have specific functional implications that warrant further investigation.

We conclude this section on the morphological parameters of muscle function with a caveat. As noted by Taylor and Vinyard (2004), caution should be exercised when testing evolutionary hypotheses regarding musculoskeletal functional morphology with "natural experiments" among different species because muscle architecture is plastic and therefore not necessarily a direct product of a heritable genotype. First, muscles do not exhibit uniform responses to increased high force exercise: rabbit feeding musculature increases PCSA through gains in mass while fiber length and pennation remain constant (Taylor et al., 2006), whereas mouse forelimb muscles exhibits variable gains in mass while consistently increasing PCSA and decreasing fiber length (Rabey et al., 2015). Second, fiber length increases in response to increasing resting length, moment arm, eccentric loading behaviors, and high velocity exercise (Williams and Goldspink, 1973; Koh and Herzog, 1998; Butterfield et al., 2005; Rabey et al.,

2015). Recent experimental evidence suggests that bony attachment site morphology is not responsive to changes in loading conditions over the course of several weeks (Zumwalt, 2006; Rabey et al., 2015), and therefore we can assume that mechanical advantage is not plastic. In light of the evidence for muscle plasticity, physiological adaptation needs to be accounted for when making claims that a muscle's morphology is a product of adaptation by natural selection. Indeed, muscle plasticity likely plays a significant role in the evolution of musculoskeletal design. By altering force, range of motion and velocity, or both through changes in fiber morphology in response to organismal behavior, muscle plasticity can create the conditions in which natural selection may favor a different, less plastic mechanical advantage as new behaviors emerge (Anapol and Barry, 1996).

#### **Activity Patterns and Physiology**

Morphological studies are necessary but not sufficient for studying musculoskeletal function because the nervous system can activate muscles to variable degrees and under various physiological conditions. The flexibility of the nervous system, termed the neurological "wildcard" by Lauder (1995), highlights the need for in vivo validation to establish that a given morphology consistently aligns with a given function. While in vivo studies are ideal, more controlled in situ and in vitro experiments serve a vital role in guiding in vivo research by highlighting the physiological principles that determine how the timing and magnitude of central nervous system output affects muscle force and velocity. This section is not a comprehensive review of the physiological determinants of function; rather, we focus on how the timing of fiber activation relative to whole muscle length change and its associated proprioceptive feedback allows the nervous system to affect, and even amplify, musculoskeletal output to mitigate the tradeoffs and constraints between force and velocity. Specifically, we discuss the benefits of active muscle stretch-eccentric activation—and mechanisms that decouple fiber and whole muscle length.

Eccentric activity is commonly conceived as detrimental to performance due to its capacity to induce muscle damage under novel exercise conditions (Lieber et al., 1991; Lieber and Fridén, 1993; Clarkson and Hubal, 2002). However, controlled eccentric activity immediately prior to shortening, termed a stretch-shortening cycle (SSC) or countermovement, increases shortening force (Abbott and Aubert, 1952; Cavagna et al., 1968; Cavagna and Citterio, 1974; Gregor et al., 1988; Finni et al., 2000). An abundance of evidence suggests that elastic energy storage in tendons and titin-a large, calciumdependent, spring-like protein spanning half of the sarcomere-underlies the enhanced and increased metabolic efficiency of force production during SSCs and may actually protect the sarcomeres from damage during whole muscle stretch (Edman et al., 1978; Roberts et al., 1997; Biewener et al., 1998; Journa et al., 2008; Leonard et al., 2010a,b; Nishikawa et al., 2012; Joumaa and Herzog, 2013; Azizi and Roberts, 2014; Holt et al., 2014; Konow et al., 2015; Monroy et al., 2016; Powers et al., 2016; Pace et al., 2017). Indeed, Herzog and colleagues (1993, 2015) argue that titin should be considered a third myofilament alongside actin and myosin due to its

substantial contributions to force production during active fiber lengthening. Muscles of variable architecture exhibit SSCs during cyclic behaviors *in vivo* (Biewener et al., 1998; Altringham and Ellerby, 1999; Nelson and Jayne, 2001; Soman et al., 2005; Higham et al., 2008; Aiello et al., 2013), suggesting that SSCs may be a common mechanism of enhancing force production (Biewener, 1998). Although titin offers a promising mechanistic explanation for increased performance associated with SSCs, the ultimate cause of enhanced power *in vivo* is still contested (Van Hooren and Zolotarjova, 2017).

Muscle stretch may also facilitate performance due to changes in the length-tension curve associated with submaximal activation. Architecture-based arguments assume that the force-length relationship is independent of muscle activation level; however, in situ and in vitro studies show that optimal length increases as activation level decreases (Rack and Westbury, 1969; Roszek et al., 1994; Holt and Azizi, 2014; but see de Brito Fontana and Herzog, 2016 for conflicting in vivo data). The effect of activation level on in vivo muscle force and velocity is poorly understood and may contribute to the difficulty of accurately modeling submaximal force production in silico (Perreault et al., 2003; Wakeling et al., 2012; Lee et al., 2013; Millard et al., 2013; Dick et al., 2017).

To relate submaximal activation to morphology and SSCs, the ability to stretch a muscle prior to shortening should improve performance because optimal length is longer during submaximal activation. Similarly, the inability to stretch a submaximally activated muscle imposes a constraint that leads to suboptimal performance under certain circumstances. In the cane toad, a crouched posture and flexed knees prior to hopping does not allow the primary ankle plantarflexor, the plantaris, to reach its optimal length for submaximal activation (Holt and Azizi, 2016). Although it shortens at a velocity that optimizes power for the force that it does produce, the plantaris nonetheless does not function optimally during submaximally active hops due to a morphological constraint: the inability to further stretch the muscle when the hindlimb is in its fully flexed position prior to the hop (Holt and Azizi, 2016). Although the cane toad is not able to capitalize on stretch-shortening cycles to enhance force or velocity during hopping, other species of anurans utilize a separate method to enhance muscle power: tendon elasticity returns energy faster than it is stored to amplify power (Roberts et al., 2011; Astley and Roberts, 2012; Astley and Roberts, 2014). Elastic recoil also underlies ballistic tongue projection in salamanders and chameleons, another system in which countermovement prior to shortening is limited (Deban et al., 2007; Anderson and Deban, 2010; Anderson, 2016).

Tendon elasticity is one of two mechanisms bypassing architectural tradeoffs by decoupling fiber kinematics from whole muscle kinematics. While *in vitro* studies suggest that active whole muscle length-tension relationships can be modeled as scaled sarcomeres during isometric contraction regardless of architecture (Winters et al., 2011), such modeling does not account for the fact that in *in vivo* dynamic conditions fiber length can be decoupled from whole muscle length. Decoupling mechanisms include fiber rotation in pennate muscles and the aforementioned elastic tissue strain in muscles with internal or external tendons.

In vitro studies have demonstrated that increased fiber rotation leads to increases in the ratio of muscle belly velocity to fiber velocity (architectural gear ratio, AGR). A muscle's AGR is not fixed during either shortening or lengthening but rather is dependent on loading conditions (Azizi et al., 2008; Azizi and Roberts, 2014), violating a fundamental assumption of architectural predictions of the effective range of motion in pennate muscles (Zajac, 1989). However, fiber rotation offers little benefit to muscle power because muscle velocity increases at the expense of force.

In contrast, decoupling fiber length from whole muscle length through tendon strain can greatly amplify whole muscle power. Because tendons can return stored energy more quickly than the duration of the initial stretch, muscles with pennate architecture and long tendons may produce higher velocity and higher powered movements than would be expected from their fiber architecture alone (Roberts et al., 1997; Aerts, 1998; Henry et al., 2005; Soman et al., 2005; Deban et al., 2007; Anderson and Deban, 2010; Astley and Roberts, 2012; Astley and Roberts, 2014; Sawicki et al., 2015; Anderson, 2016; Roberts, 2016). Moreover, estimates of fiber length from whole muscle length must assume that tendons are stiff; consequently, contributions of internal and external tendon strain are ignored, potentially neglecting significant contributions of elastic energy storage to performance or protecting sarcomeres from excessive stretch (Zajac, 1989; Soman et al., 2005; Lieber, 2009; Konow et al., 2015; Roberts, 2016). Therefore, the morphology of the muscle fibers should be considered in tandem with the internal and external tendon morphology in functional arguments (Anapol and Barry, 1996; Biewener, 1998; Anapol and Gray, 2003).

Brief mention is warranted of other important morphological and physiological processes that affect muscle function but are beyond the scope of this review. Body size introduces another level of complexity to musculoskeletal functional morphology due to the negative allometry of force production to body mass (e.g., Biewener, 1989; Biewener, 1990). The effects of scaling extend to not only the duration of vertebrate locomotor and feeding cycles—and therefore potentially to the relative velocity of muscle fibers—but also the timing of muscle activation in appendages large enough to utilize momentum for movement (Pennycuick, 1975; Pontzer, 2007; Hooper et al., 2009; Ross et al., 2009; Gintof et al., 2010; Hooper, 2012; Ross et al., 2017). Cycle duration, musculoskeletal design, and the spring-like properties of muscle-tendon units may also function to reduce energy expenditure and fatigue (Taylor, 1985; Cavagna et al., 1997; Marsh et al., 2004; Raichlen, 2004; Modica and Kram, 2005; Hunter and Smith, 2007; Pontzer, 2007; de Ruiter et al., 2013; Kilbourne and Hoffman, 2013, 2015), and some organisms may be optimized for submaximal activations and endurance at longer fiber lengths rather than maximal activations and power at "optimal" fiber lengths. Lastly, we have focused exclusively on motor output; however, sensory input (e.g., proprioception) is equally important for the performance of musculoskeletal structures (Dickinson et al., 2000; Nishikawa et al., 2007). Elements of biomechanical design correlate with sensory function and the morphology of peripheral sensory receptors, and integrating evidence of sensory "tuning" to a given function may be instrumental in

supporting or falsifying functional hypotheses (Aiello et al., 2017). For example, the mechanoreceptors of isometrically active muscle with stiff tendons may be more sensitive than those of concentrically or eccentrically active muscle with more compliant tendons.

### INTEGRATIVE APPROACHES

Morphological and physiological studies have been instrumental to the advancement of our understanding of muscle function. However, for the reasons discussed above, morphology does not have a one-to-one correspondence with function, and the tightly controlled conditions of many laboratory experiments are not reflective of how muscles are used during natural behavior (Gregor et al., 1988). Therefore, the strongest evidence to support or falsify adaptive hypotheses of musculoskeletal function derives from in vivo experimental studies (Lauder, 1996; Ross et al., 2002). Although in silico modeling offers a promising alternative to costlier in vivo experiments, these models struggle to produce accurate results under dynamic, submaximal conditions (Perreault et al., 2003; Wakeling et al., 2012; Lee et al., 2013; Millard et al., 2013; Dick et al., 2017). In silico model parameters are commonly based on static length-tension curves and force-velocity curves derived from isometric and isotonic activity (Zajac, 1989). However, submaximally active muscles have longer optimal fiber lengths (Rack and Westbury, 1969; Roszek et al., 1994; Holt and Azizi, 2014; Holt and Azizi, 2016), and submaximal stretchshortening cycles allow organisms to produce forces greater than that predicted by a supramaximally stimulated isotonic force-velocity curve (Gregor et al., 1988). Thus, determining how morphology and physiology interact through in vivo study of natural behavior is necessary to improve our ability to both accurately model and understand muscle function. Specifically, whether and how variation in fiber type, activity patterns, historydependence (e.g., SSCs), and decoupling mechanisms contribute to the difficulties of modeling muscle force is poorly understood. This section discusses additional dynamic processes that could underlie modeling inaccuracies including moment arm and axis of rotation dynamics, interactions, muscle morphological synergist and heterogeneity—and methodological approaches that may resolve these issues by integrating morphological and physiological lines of evidence.

# Dynamic Interactions between Morphology and Physiology

Although a muscle's moment arm is primarily dependent on the distance of its attachment points from the center of rotation, mechanical advantage is also dependent on skeletal posture and the center of rotation (Biewener, 1989; Herzog and Read, 1993; Loren et al., 1996; Gonzalez et al., 1997; Kargo and Rome, 2002; Iriarte-Diaz et al., 2017). Additionally, because organisms adopt different postures for different behaviors, e.g., human walking vs running, a given muscle's mechanical advantage can be dynamic not only within behaviors but among them as well (Biewener et al., 2004), which may contribute to changes in muscle function with changes in gait (Gregor et al., 1988; Arnold et al., 2013). Dynamic models of a variety of vertebrates

have been useful in understanding how joint moments vary due to both moment arm length and fiber length (Kargo and Rome, 2002; Hutchinson et al., 2005; Hutchinson et al., 2015; Charles et al., 2016a,b) and highlight how 3D approaches are necessary for measuring joint moments accurately when movements are complex, as in linkage systems (Olsen and Westneat, 2016). Interactions among moment arm length, muscle length, and posture may be particularly important when considering the function of biarticular muscles.

However, a fundamental assumption in these in silico models is the location of the joint axis of rotation, which affects the length of a muscle's moment arm and therefore how much a muscle strains during a given behavior. In the feeding systems of many mammalian species the mandibular condyle translates anteroposterior during jaw opening and closing, meaning that the axis of rotation is located inferior to the temporomandibular joint (Wall, 1999; Keefe et al., 2008; Terhune et al., 2011; Ross et al., 2012; Menegaz et al., 2015). Translation of the mandibular condyle during jaw opening and closing ameliorates the force-length tradeoff in the highly pennate masseter muscle by taking advantage of the longer fibered temporalis (Weijs et al., 1989; Iriarte-Diaz et al., 2017). In light of these in vivo data, accounting for the active (i.e., myofibrils) and passive (e.g., connective tissues) contributions to the location of the center of rotation is important to the accuracy of both moment arm and fiber length computations in silico.

As mentioned previously, specialization of synergists can facilitate the production of consistent force over a wide range of motions or velocities while decreasing overall muscle mass. In the case of the mandibular axis of rotation, joint kinematics allow the muscles of mastication to optimize force production within the constraints of their length-tension curves (Iriarte-Diaz et al., 2017). However, counterintuitive to the term "synergist", high performance in one synergist may come at the expense of performance in the other. For example, the short, highly pennate, and predominantly slowtwitch fibers of the human soleus suggest that this muscle functions optimally at lower velocities, whereas the heads of the gastrocnemius have longer, less pennate, and more fast-twitch fibers (Edgerton et al., 1975; Ward et al., 2009a). The shortening velocity of soleus fibers during high-speed behaviors can exceed that of the maximum velocity of slow twitch fibers, thus rendering the soleus mechanically sub-optimal or even incompetent at high speeds (Wakeling et al., 2006). Although early studies are promising, it is unclear whether accuracy of in silico models is improved by incorporating fiber type, which warrants further investigation (Lee et al., 2013; Dick et al., 2017).

Morphological and functional heterogeneity can also be found *within* muscles in the form of variable activation patterns, fiber lengths, pennation, and fiber types. Muscles with simple morphology can thus be functionally subdivided to achieve more complex movements (Aiello et al., 2014). In muscles with regional disparity in fiber-type distribution, the orderly recruitment of smaller, slow-twitch fibers prior to larger, fast-twitch fibers in both locomotor and feeding musculature (Henneman et al., 1965; Milner-Brown et al., 1973; Goldberg and Derfler, 1977; Yemm, 1977; Clark et al., 1978; Mendell, 2005; Ross et al., 2007, 2010) probably results in

portions of muscles with different lengths, maximum velocities, forces, and moment arm lengths becoming active prior to others (Higham and Biewener, 2011). As mentioned previously, high velocities produced by fast fibers may subsequently render the slow fibers mechanically incompetent at high activation levels, thus reducing force and power further beyond the losses incurred assuming a homogeneous force-velocity relationship. Higham and Biewener (2011) offer a testable hypothesis that more homogenous muscles are more specialized in function while more heterogeneous muscles function similarly to specialized synergists by improving both motor control over a joint and mechanical performance over a wider range of postures and behaviors. Overall, morphological heterogeneity raises important questions about the definition of a muscle from a functional perspective and whether the central nervous system controls different sections of a muscle independently or if peripheral specialization simplifies motor control while increasing functional complexity (Zatsiorsky and Prilutsky, 2012).

## **Capturing Muscle Kinematics and Kinetics**

To determine how the various morphological and physiological parameters of musculoskeletal performance interact, one needs to relate muscle fiber activity to three-dimensional kinematics and kinetics of fibers (ideally from multiple regions of the same muscle), whole muscle-tendon units, and the skeleton (German et al., 2011). All of these kinematic variables can be measured simultaneously using the high-resolution methods discussed below. However, accurate measures and predictions of in vivo fiber and muscle kinetics remain elusive for certain kinds of muscles. Although the kinetics of muscles with long tendons can be obtained using buckle tendon force transducers (Barnes and Pinder, 1974; Biewener, 1992), fiber optic sensors (Finni et al., 1998), or tendon strain measurements (Dick et al., 2016), such methods cannot be applied to muscles with short or internal tendons. Strain gauges implanted on bone or near sites of bone attachment have been used to study the force production of muscles with short or no external tendons, such as the primate jaw elevators (Hylander, 1986; Hylander et al., 1987, Hylander and Johnson, 1989; Hylander and Johnson, 1993), avian pectoralis (Biewener et al., 1998; Soman et al., 2005), and testudine hindlimb musculature (Aiello et al., 2013). However, strain gauges cannot measure an individual muscle's force in isolation because their measurements are affected by activity in other muscles that attach to the same bone as well as joint and bite reaction forces. A recently developed probe capable of measuring thousands of sarcomeres in vivo (Young et al., 2017) offers a promising alternative to mechanical transducers and may help resolve the problems of modeling single muscle force from sarcomere length during non-isometric and submaximal activity. However, multiple such probes will be necessary given that fiber and sarcomere strain are heterogeneous throughout the muscle (Ahn et al., 2003; Konow et al., 2010; Wentzel et al., 2011; Holman et al., 2012; Moo et al., 2016; O'Connor et al., 2016).

Muscle kinetics are frequently integrated with synchronized recordings of skeletal kinematics from high-speed cameras and kinetics from implants or external

sensors. Systems such as Vicon (Vicon Motion Systems, Oxford UK) permit the study of rigid body kinematics, joint kinematics, instantaneous axis of rotation (which influences dynamic torque), and whole muscle length change (Reed and Ross, 2010; Ross et al., 2012; Ross and Iriarte-Diaz, 2014; Takahashi et al., 2017; Iriarte-Diaz et al., 2017). Although light-based motion capture technology can generate large data sets of multiple skeletal segments and allow assessment of the distribution of kinematic variance across species, individuals, and behaviors (Iriarte-Diaz et al., 2012; Ross et al., 2012; Iriarte-Diaz et al., 2017), it cannot provide data on internal kinematics of soft tissues such as individual fibers or structures obscured by skin (e.g., oropharyngeal structures). To measure these obscured-yet-essential kinematics, light-based motion capture must be combined with additional methods, such as sonomicrometry (e.g., Roberts et al., 1997; Biewener et al., 1998; Konow et al., 2012), ultrasound (e.g., Dick et al., 2016; Dick et al., 2017), or, the focus of this paper, biplanar x-ray imaging.

## New Approaches to Functional Morphology and Biomechanics

In the last decade two technologies have been developed that hold particular promise for advancing integrative studies in functional morphology of musculoskeletal systems: diffusible iodine-based contrast-enhanced computed tomography (diceCT) (Metscher, 2009; Gignac et al., 2016) and X-ray Reconstruction of Moving Morphology (XROMM) (Brainerd et al., 2010).

DiceCT and other non-iodine staining methods enable morphological measurements of soft-tissue morphology using non-destructive methods and with unprecedented spatial resolution. Not only does diceCT have the potential to improve our ability to measure musculo-tendon morphology, but it also enables data collection from museum specimens that were previously inaccessible to destructive techniques. Applications of diceCT and other staining methods include the digital dissection of muscles too small or complex for traditional dissection (Metscher, 2009; Jeffery et al., 2011; Holliday et al., 2013; Porro and Richards, 2017), determining muscle orientation in models of bite force (Gignac and Erickson, 2017; Sellers et al., 2017), reconstructing threedimensional muscle architecture (Kupczik et al., 2015; Dickinson et al., 2018), and improving the accuracy of inverse dynamic modeling of joint moments (Charles et al., 2016a,b). One of diceCT's key strengths in muscle functional morphology is its potential to measure muscle architecture in situ, which may generate more accurate measures of joint moment if architecture varies along the length of the muscle's attachment site. Meanwhile, methods of digitally determining muscle architecture are promising and continue to improve (Kupczik et al., 2015; Dickinson et al., 2018).

X-ray Reconstruction of Moving Morphology (XROMM, Brainerd et al., 2010) and its corollary fluoromicrometry (FMM, Camp et al., 2016) capture internal musculoskeletal kinematics with high spatiotemporal resolution and can be integrated with workflows to estimate force output by individual muscles. XROMM measures the 3D rotation and translation of rigid tissues such as bone whereas FMM measures the 3D deformation of soft tissues. Studies using XROMM and FMM

have made significant progress in the field of muscle functional morphology, demonstrating that suction feeding in largemouth bass is powered primarily by axial rather than cranial musculature (Camp and Brainerd, 2014; Camp et al., 2015; Camp and Brainerd, 2015), the length-tension curve constrains the performance of structures that lack joints and the benefits of mechanical advantage, as in carp pharyngeal jaws (Gidmark et al., 2013), and tendon elasticity decouples fiber and joint kinematics to power frog hopping through a catapult-like mechanism (Astley and Roberts, 2012; Astley and Roberts, 2014).

## Combining diceCT, XROMM, and EMG

Together, diceCT and XROMM promise to increase the depth of knowledge about musculoskeletal design in unprecedented ways. Given the many determinants of function discussed above, methods that discern how individual fibers and muscles each contribute to a given movement are necessary to fully understand how muscles function with the skeleton to produce force and movement. The remainder of this article describes how incorporation of diceCT into the XROMM workflow can enhance the study of muscle kinematics, particularly in musculoskeletal systems that are difficult to access for surgical implantation of muscle markers.

Previous studies have integrated XROMM and kinetic or EMG measurements in a limited number of muscles to relate muscle behavior to skeletal outputs by implanting individual muscles with tantalum beads or by reconstructing their attachments on bone from osteological landmarks (Astley and Roberts, 2012; Gidmark et al., 2013; Camp et al., 2015; Konow et al., 2015). We demonstrate how diceCT can be incorporated into XROMM and EMG workflows to study over a dozen muscles, many of which are difficult to access surgically for FMM. Moreover, because in silico studies have demonstrated that measures of joint moment are sensitive to the accuracy of muscle attachment site location (Hutchinson et al., 2015; Charles et al., 2016b), we demonstrate the sensitivity of XROMM-based muscle kinematics to variation in attachment site location. We also demonstrate that these methods are precise enough to measure in vivo muscle fiber linear and angular velocity in our model system, the hyolingual apparatus of the rhesus macaque (Macaca mulatta).

The benefits of integrating XROMM, diceCT, and EMG are especially salient for investigations of vertebrate feeding systems. Jaw and hyolingual musculature are redundant, have variable architecture and, in many species, execute their functional promiscuity within the limited space sampled by the capture volume of XROMM. Moreover, the complex, three-dimensional orientations of feeding system muscles, as well as the three-dimensional movements and shape changes of the hyolingual apparatus (Kier and Smith, 1985; Pearson et al., 2011; German et al., 2011) are obscured by the tissues of the head and neck. Therefore, skeletal, lingual, and muscle kinematics can currently only be studied simultaneously and with high spatiotemporal resolution using these radiography-based techniques, which have been successfully applied to feeding in several vertebrate species (Gidmark et al., 2013; Camp and Brainerd 2014; Gidmark et al., 2014; Camp and Brainerd 2015; Camp

et al., 2015; Gidmark et al., 2015; Menegaz et al., 2015). Thus, the field of vertebrate feeding functional morphology stands to reap significant benefits from XROMM, FMM, diceCT, EMG, and their integration.

The data presented here were collected as part of an on ongoing research program to develop a nonhuman primate model of human swallowing biomechanics (Nakamura et al., 2017). Previous studies have measured hyolingual kinematics (Franks et al., 1984; German et al., 1989; Hiiemae et al., 1995; Steele and Van Lieshout, 2008; Matsuo and Palmer, 2010; Nakamura et al., 2017), individual muscle activity (Inokuchi et al., 2014, 2016), muscle length (Okada et al., 2013; Feng et al., 2015), and simultaneous skeletal kinematics and EMG (Palmer et al., 1992; Park et al., 2017), but this is the first study to integrate EMG with in vivo 3D measures of both hyolingual kinematics and muscle length, orientation, and velocity. Specifically, this article demonstrates how integration of these techniques can be used to evaluate the mechanisms underlying hyoid elevation during chewing and swallowing (Fig. 1). Mylohyoid (especially the posterior mylohyoid, which inserts into the hyoid itself), anterior and posterior digastrics, and stylohyoid are hypothesized to be key elevators of the hyoid (Pearson et al., 2011). Although usually thought of as a tongue retractor or depressor in humans (Pearson et al., 2016; Standring, 2016), the hyoglossus in macaques (and humans) is also somewhat superiorly oriented and could also elevate the hyoid (Matsuo and Palmer, 2010). The set of muscles potentially involved in hyoid elevation have variable architecture, including bipennate (posterior digastric), unipennate (anterior digastric), and parallel-fibered (mylohyoid, stylohyoid, and hyoglossus); therefore, hyoid elevation serves as a useful example of how these methods can be used to examine behavior and function among muscles with different morphologies.

## **METHODS**

Marker-based XROMM involves two data collection workflows (Brainerd et al., 2010); integration of XROMM with diceCT adds a third (Fig. 2).

#### **Animal Subjects**

Data from two adult rhesus macaques (*Macaca mulatta*, one male, one female) were used to develop these methods. These two animals had previously been used in neurophysiological experiments involving neural array implantation in limb areas of somatosensory cortex, parietal cortex, and premotor cortex not obviously related to hyolingual function.

The methods described were a part of an IACUC-approved protocol at the University of Chicago. The animals were housed at an on-campus, AAALAC-accredited animal facility attended to daily by veterinary and husbandry staff. The animals were trained to feed while sitting in an XROMM-compatible, acrylic primate chair. The animals were trained to be transferred to and from their cages by a pole-and-collar system.

On non-training days, animals were fed monkey biscuits and given daily enrichment along with *ad libitum* access to water. On training days, the animals were sometimes food and water delayed until after data collection to encourage them to eat during the session.

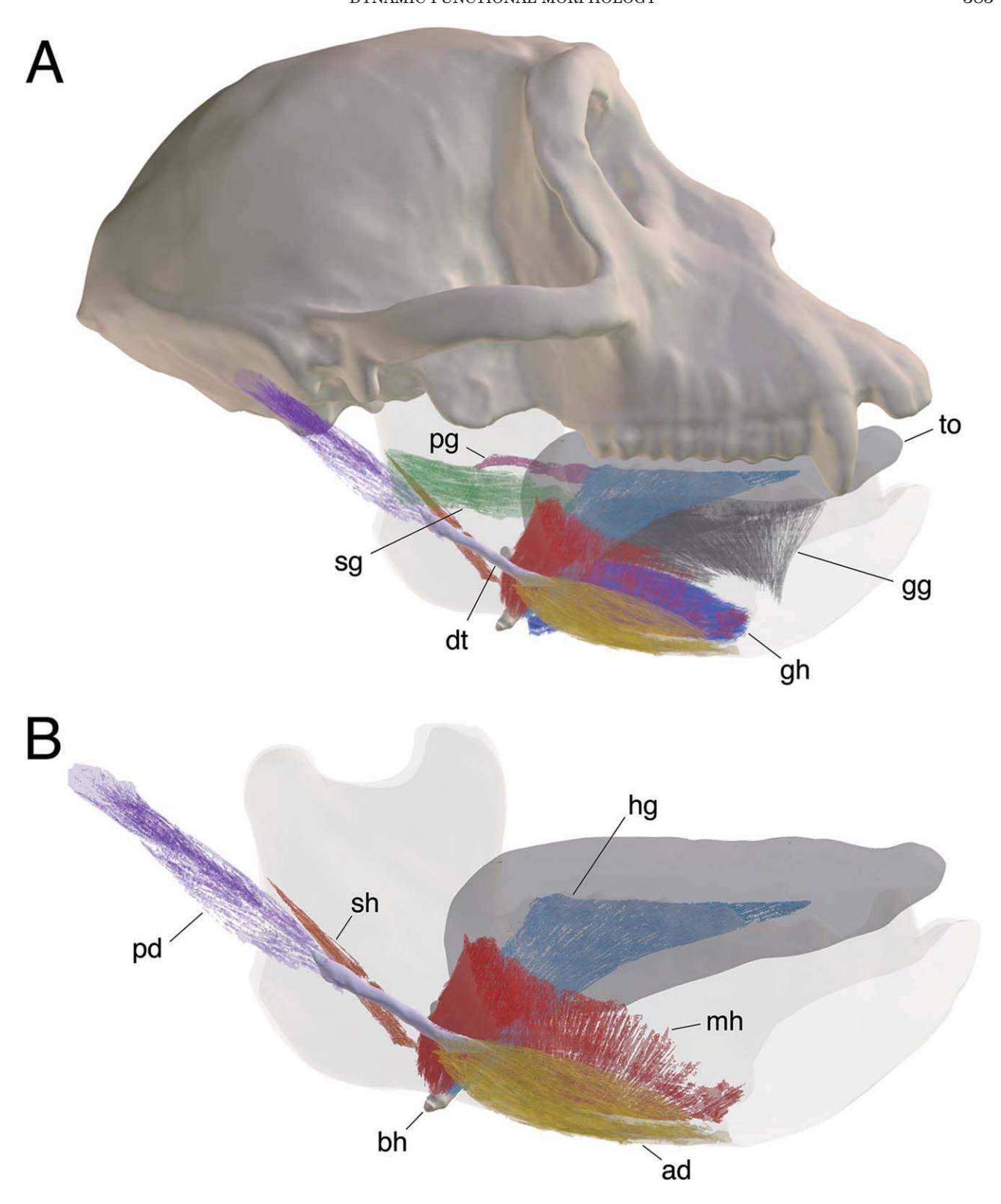


Fig. 1. Select macaque hyolingual muscles. (A) Lateral view of cranium, mandible (transparent), basihyoid, and select hyolingual muscles in Monkey J. The kinematics of these muscles were reconstructed using a combination of XROMM and FMM. (B) Same view as A, showing only the muscles that are hypothesized to produce hyoid elevation. Abbreviations (color): ad, anterior digastric (yellow); bh, basihyoid (tan); gg, genioglossus (dark gray); gh, geniohyoid (blue); hg, hyoglossus (light blue); mh, mylohyoid (red); pd, posterior digastric (purple); pg, palatoglossus (pink); sg, styloglossus (green); sh, stylohyoid (orange); to, tongue (light gray).

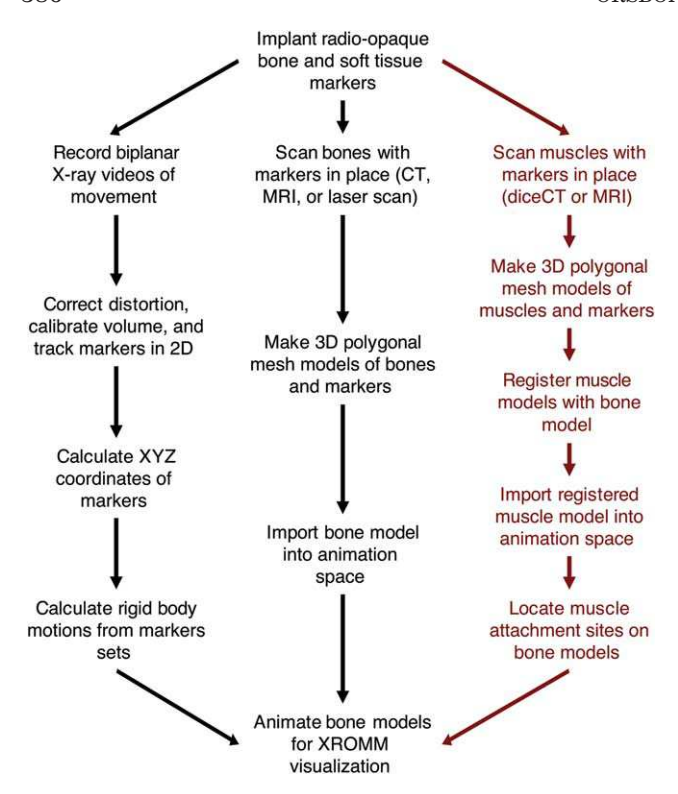


Fig. 2. XROMM-diceCT workflow. The described method integrates XROMM (Brainerd et al., 2010) and diceCT (Gignac et al., 2016) workflows to determine the relationships among muscle, bone, and implanted markers. Figure modified from Brainerd et al., 2010.

#### **Surgical Implantation**

We developed a surgical approach to implant 1.0 mm tantalum markers in the primate cranium, mandible, hyoid body, and orofacial soft tissues that builds on that described by previous XROMM studies of the mammalian feeding system (Brainerd et al., 2010, Menegaz et al., 2015), and developed methods for implanting electromyographic (EMG) fine-wire electrodes in hyolingual muscles for chronic recordings (up to seven months).

Tantalum beads were inserted into the cranium and mandible by making an incision in the skin, clearing away a small area of periosteum, and drilling a 1-2 mm deep hole into the bone with a hand drill and a 1.0 mm drill bit, and then press-fitting a tantalum bead into the hole. Tantalum beads were inserted into the hyoid by locating two exposed portions of bone at the inferior pole of the hyoid body and inserting markers in a similar manner as in the cranium and mandible. A third marker was placed in the midline of the hyoid body after dividing the mylohyoid raphe and gently blunt dissecting the fibers of geniohyoid to visualize the midline of the bone. A marker was then inserted as stated above. Following marker insertion, the cut ends of the mylohyoid raphe were sutured back together using 4-0 absorbable suture. Markers were inserted into soft tissues using a 16-gauge angiocatheter in the following manner: a needle introduced the catheter, the needle was withdrawn, a marker was placed into the catheter, a spinal needle stylus was used to hold the marker in the tissue as the catheter was removed by drawing it backwards over the stylus,

and finally the stylus was removed while applying pressure to the insertion site. If necessary to achieve hemostasis, or to prevent the marker from falling out, the incision was sutured closed using 4-0 Vicryl suture.

electromyography, we implanted insulated, medical-grade stranded stainless steel fine-wire electrodes (Cooner Wire, Chatsworth CA). A 27-pin connector (Omnetics Connector Corporation, Minneapolis MN) was housed in a custom-built, percutaneous, titanium housing that was rigidly fixed to the cranium using bone screws. The EMG connector allowed for recording from 13 muscles using four differential amplifiers (Model 1700, AM Systems, Sequim WA), and the 27th wire remained implanted under the skin as a ground wire. The wires were tunneled subcutaneously to the submandibular area and 1-2 mm of insulation was stripped. Electrodes were implanted into the muscle using an 18or 20-gauge needle and were stimulated through the connector intraoperatively to confirm their location (single stimulation, train rate = 1 Hz, train duration = 300ms, stim rate = 250 pulses per second, delay = 0.01 ms, duration = 0.2 ms, voltage = 5-10 V, Grass S48 Stimulator, AstroNova, Inc., West Warwick RI).

The animals were given intramuscular buprenorphine for two days and cephalosporin antibiotics for five to seven days following the surgery. We waited two weeks prior to collecting data to allow healing and the formation of scar tissue around the markers that fixes them in place relative to the surrounding tissue.

These procedures have been replicated six times and, by fluoroscopically observing the animals swallowing contrast-enhanced liquids mixed with fruit juice (240 mg/ml iohexol and 60% w/v barium sulfate), we were able to find no evidence of chronic swallowing pathology as a result of these procedures.

#### In Vivo Data Collection and Sacrifice

Kinematic and precision data presented here were collected in the University of Chicago's XROMM Facility (https://xromm.uchicago.edu/). This custom-designed facility features the high speed biplanar videofluoroscopy equipment necessary for XROMM and FMM (Brainerd et al., 2010, Camp et al., 2016), differential amplifiers for EMG (AM Systems Model 1700) and a video processing unit (XCitex ProCapture VPU) that synchronizes the two data sources. Prior to data collection, the capture volume was spatially calibrated using undistortion grids and a calibration cube (Brainerd et al., 2010). The monkeys were trained to eat a variety of foods, including the red grapes with skin reported here, presented to them using tongs while they were seated in a primate chair situated in the XROMM capture volume. X-ray video data were collected at 90-100 kVp, 10-16 mA, 200 Hz, and with a 2,000-4,000 ms shutter speed, balancing the need to minimize motion blur, data size, X-ray tube heat, and animal X-ray exposure. The EMG signals presented here for Monkey J were collected at 2,000 Hz, amplified 100-10,000×, and filtered (60 Hz notch, 100–1,000 Hz bandpass).

Following a separate terminal experiment, the animals were perfused under deep anesthesia with 0.5 to 1.0 L of saline plus heparin sodium (10 IU/mL) followed by 1.0 to 2.0 L 10% formalin solution, infused under pressure through the left ventricular cannula, and sacrificed via exsanguination.

TABLE	1.	uCT scan	parameters
-------	----	----------	------------

Parameter	Monkey K (unstained)	Monkey K (diceCT)	Monkey J (unstained)	Monkey J (diceCT)
kVp	200	200	205	215
mÂ	400	185	200	300
Exposure time (ms)	500	1,000	250	500
Skipped exposures	1	1	1	1
Exposures averaged per image	3	3	3	3
Images per scan	2,000	2,000	2,000	2,000
Voxel width (μm) <sup>a</sup>	90.517	37.000	91.082	64.506
Filter (size and element)	none	0.5 mm Sn	0.5 mm Cu	0.5 mm Sn

<sup>&</sup>lt;sup>a</sup>All three voxel dimensions were equal.

## **Generating XROMM Bone Models**

After sacrifice, the head and neck were placed in a 20 L bath of 10% formalin solution for at least seven days to fix the tissue. The stained and unstained carcasses were scanned in the PaleoCT at the University of Chicago, a General Electric Phoenix v tome x Microfocus CT (microCT) scanner. Scanning parameters for unstained and stained specimens can be found in Table 1. For each animal, tantalum markers and bone models were segmented to create polygonal mesh models using Amira 5.5.0 (FEI Company, Hillsboro OR) hosted on a visualization node of the Research Computing Center at the University of Chicago. Minimally smoothed outputs from Amira were used when locating landmarks for kinematic measurements. To generate the figures presented here, a shell was created using 3-matic Research v10.0 (Materialise, Leuven, Belgium). The shells were subsequently smoothed and metal implants and artifacts were removed using Autodesk ReMake 2016 (Autodesk, San Rafael CA).

## DiceCT

After the precision experiment discussed below, the carcasses were placed in a 5 liter 20% weight/volume sucrose solution prewash to minimize tissue shrinkage during staining (Morhardt et al., 2016). Following the prewash the carcasses were placed in either a two liter (Monkey K) or three liter (Monkey J) 1.25% I<sub>2</sub>/2.50% KI solution made by diluting a 5% I<sub>2</sub>/10% KI stock solution with deionized water. Short (five to ten minute) microCT scans were conducted every two to four weeks to evaluate staining progress. After at least two weeks in 1.25% I<sub>2</sub>/2.50% KI solution, the carcasses were transferred to a 2% I<sub>2</sub>/4% KI solution that was replenished every two to four weeks until staining of the center of the specimen was observed on the interval CT scans. After the iodine penetrated to the center of the specimen, the carcasses were placed in a deionized water bath for 2-4 days to even the contrast throughout the specimen before the final microCT scan.

## Segmentation and Registration

The diceCT data set was segmented using Amira 5.5.0. When segmenting, fascicles were defined as the high-density material (muscle fibers and endomysium) surrounded by lower density material (perimysium). Low-density tissues below a minimum gray-scale value threshold were excluded from the segmented volume.

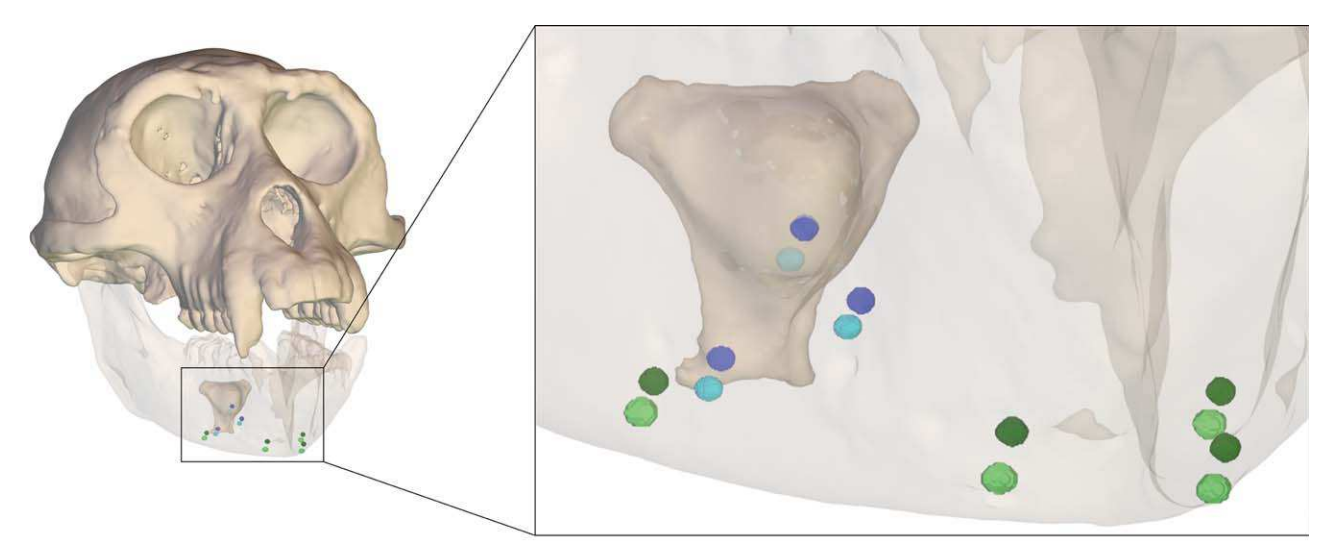
Because voxel width approximated the reported diameter of macaque styloglossus fibers (37.0–64.5  $\mu m$  versus ca. 40–90  $\mu m$ , respectively), no distinction could be made between fibers or between fibers and endomysium (Sokoloff et al., 2007). For the geniohyoid and posterior mylohyoid, the fascicles immediately adjacent to the bare ends of the EMG electrodes were segmented. For stylohyoid, palatoglossus, and the posterior digastric, the entire muscle was segmented. For hyoglossus, genioglossus, styloglossus, and anterior digastric, only the fascicles containing or most closely related to an implanted marker were segmented. Additionally, the tantalum markers in the cranium, mandible, and hyoid were segmented for registration with the unstained bone model dataset.

When transforming the muscle models into the bone model coordinate systems, models of each bone's tantalum markers from each data set were registered using the AffineRegistration function in Amira. The unstained CT data set was set as the "Reference" and the stained CT data set was set as the "Model". The transformation matrix used to align the stained CT model with the unstained CT model was then applied to the stained CT muscle models, and the transformed muscle models were exported as .obj files. Because tissue deformation during iodine staining moved the hyoid and mandible relative to the cranium (Fig. 3), separate models were made using bone-specific transformation matrices. Specifically, two models were generated for the posterior mylohyoid, geniohyoid, and stylohyoid. One model in the coordinate system of the bony attachment was created for each of the following muscles: styloglossus, hyoglossus, genioglossus, and anterior and posterior digastrics.

Tissue shrinkage has been observed in muscle following iodine staining (Vickerton et al., 2013) but to our knowledge the effects on bone morphology have not been quantified. The registered marker models were also exported as .obj files and imported into Autodesk Maya 2016 (Autodesk, San Rafael CA). The vAvg function of XROMM Maya Tools v2.1.8 was used to calculate their centroids. To quantify the error introduced by both skeletal tissue shrinkage and using either cranial or bone-specific registrations for muscle models, the mean intermarker distance between homologous markers was calculated for each bone (Table 2).

### **Defining Muscle Attachment Sites**

After creating registered muscle models, the models were imported into Autodesk Maya to determine the location of the fascicles' attachments on the bones (Fig. 4).



## Key

- Hyoid markers, hyoid registration
- Hyoid markers, cranium registration
- Mandible markers, mandible registration
- Mandible markers, cranium registration

Fig. 3. Data set registration. Maya rendering of macaque cranium, mandible (translucent), basihyoid, and registered markers from the diceCT scan in anterolateral view. Registering by using the transformation matrix for the cranial markers for all bones instead of bone-specific transformation matrices introduces additional error. Markers from the original scan are not shown because they nearly completely overlap markers in lighter shades (Table 1).

TABLE 2. Precision study and *in vivo* intermarker distance standard deviations

	Int	ermarker di	stance SD (cn	n)
	Monk	ey K	Monk	ey J
Bone	Precision study	In vivo	Precision study	In vivo
Cranium Mandible Hyoid	0.007 0.010 0.005	0.007 0.006 0.010	0.004 0.003 0.003	0.008 0.005 0.049

The vertices on the bone surrounding the muscle at its attachment point were selected. Some muscle fascicles did not directly insert into bone (e.g., if a fascicle inserted into a tendon that contrasts poorly with the surrounding tissue), which prompted the development of a method to determine the attachment point of these muscles. Autodesk Maya's modeling capabilities were used to create cylindrical polygons to bridge the gap. These cylinders were manually adjusted to have the approximately same diameter and orientation as the terminal end of the fascicle and extended to the bone where the connective tissue was assumed to attach. After creating a ring of identified vertices around the fascicle attachment site, the vAvg function of the XROMM Maya Tools was used to calculate the XYZ location of the attachment site centroid. For muscles that attach to bone a separate muscle model for

each attachment site was generated using bone-specific transformation matrices.

Styloglossus required specialized reconstruction because it inserts into soft tissue (the stylomandibular ligament) and not directly to the rigid cranium. The attachment sites of the ligament at the styloid area and mandible were segmented and ligament length was defined as the Euclidean distance between the two. A cylindrical polygon was used to simulate the stylomandibular ligament and another cylinder bridged the gap between the segmented styloglossus fascicles and the ligament. To define the styloglossus attachment site, an XYZ locator was manually placed at the intersection between the reconstructed ligament and the gap-filling cylinder. The distance from the reconstructed attachment site to the styloid process was normalized by ligament length to create a ratio defining how far along the stylomandibular ligament the styloglossus inserted. The ligament was reconstructed as a vector with the tail at the styloid process and the head at the mandibular ligament. The instantaneous styloglossus attachment location was reconstructed as the XYZ coordinate of the head of the dot product of the stylomandibular ligament vector and the above ratio. This method assumes that strain is homogenous throughout the ligament and that the ligament neither curves around other structures or buckles.

All muscle measurements in this study were taken from the right side, except for palatoglossus because the markers in the right palatoglossus were extruded during healing.

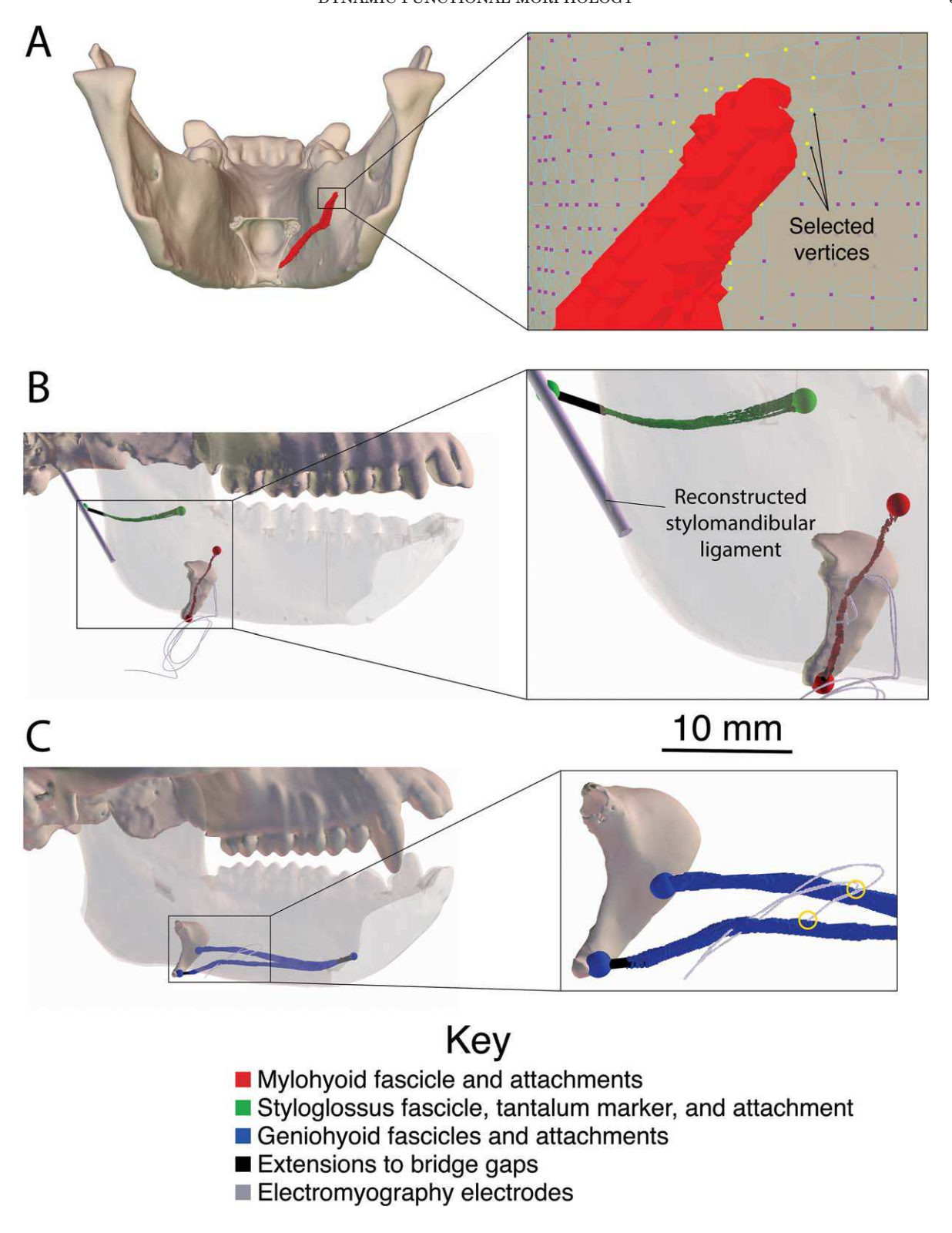


Fig. 4. Reconstructed muscle fascicles and attachment sites. (A) Rendered posterior view of the mandible, basihyoid, and mylohyoid fascicle. The inset focuses on the mylohyoid's mandibular attachment site in Maya's "vertex" mode. The model's vertices are shown in purple, and the vertices surrounding the mylohyoid's attachment on the mandible have been selected (yellow) for calculation of the attachment site. Vertices are enhanced in size. (B) Styloglossus (green) and mylohyoid (red) reconstructions (see Methods and Materials for details about reconstructions). (C) Geniohyoid reconstruction, demonstrating that the electrodes were more widely spaced in this muscle. Gold circles indicate where electrodes insert into the fascicles. The fascicles immediately surrounding the bare end of each electrode were segmented and modeled, and geniohyoid measurements were taken as the average of the results for the two groups of fascicles. Colored spheres are reconstructed attachment points, except for the anterior green sphere which was a digitized tantalum marker implanted in the styloglossus. Scale bar is for insets of B and C.

## **Digitizing**

The biplanar X-ray videos were saved as .avi files for storage and converted to .tiff stacks locally for digitization using ImageJ v1.51a (National Institutes of Health, Bethesda MD). All videos were undistorted, calibrated, and digitized using XMALab v1.4.0 (Knörlein et al., 2016), which generates both the XYZ coordinates of individual markers and rigid body transformations for markers assigned to the same bone. The XYZ coordinates and transformation matrices were filtered at 20 Hz after visually confirming in XMALab's built-in plotting features that this frequency did not over-smooth the data.

## **Defining Coordinate Systems**

Two coordinate systems were created, one fixed to the cranium and another fixed to the mandible. The cranial coordinate system was aligned such that the XZ plane was parallel to the occlusal surface of the maxillary tooth row (positive X= anterior, positive Y= dorsal, positive Z= right, after Menegaz et al., 2015) and the origin was set on the posterior nasal spine. The mandibular coordinate system was also aligned such that the XZ plane was parallel to the occlusal surface of the mandibular molars and the origin was set halfway between the mandibular condyles.

These coordinate systems can be created manually using the XROMM Maya Tools shelf (Brainerd et al., 2010) or computationally using the XYZ coordinates of the landmarks on the bones; this study used the latter method using custom-written scripts in R (R Core Team, 2017). When computationally creating coordinate systems, the maxillary and mandibular molar tooth cusps, the posterior nasal spine, and the medial-most aspect of the mandibular condyles were digitized using the vAvg function of the XROMM Maya Tools. In these macaques, the four cusps (hypocone, metacone, paracone, and protocone) on the three maxillary molars (M1, M2, M3) were used, and the four cusps (hypoconid, metaconid, entoconid, protoconid) on the three mandibular molars (m1, m2, m3) were used, in addition to the hypoconulid on the m3.

The in vivo movements of these landmarks in 3D space were reconstructed by applying rigid body transformation matrices exported from XMALab to the XYZ coordinates of the cusp landmarks to every frame. Two datasets were then created by subtracting the XYZ coordinates of the cranial and mandibular origin from the XYZ coordinates of the tooth cusps. The prcomp function of the stats package in R (R Core Team, 2017) was used to run a principle components analysis (PCA) on the location of the tooth cusps that returns a rotation matrix to align the cusps along their principle axes of variation. The first, second, and third eigenvectors define anteroposterior, mediolateral, and superoinferior, respectively, as confirmed by plotting and visually inspecting the transformed data. The rotation matrix generated by the PCA was then applied to all of the markers in the cranial and mandibular datasets-including the originally tracked tantalum markers as well as the reconstructed bone, tooth, and muscle landmarks—to create datasets describing marker location relative to the cranium and the mandible. Each dataset was then imported into Maya and animated to visually confirm that no mathematical errors had occurred.

Mandibular tooth cusps were used to calculate mandibular pitch (Z-axis rotation, mandible elevation and depression), yaw (Y-axis rotation, mandible transverse movement), and roll (X-axis rotation, mandible roll). The positions of the mandibular tooth cusps were first calculated within a cranial coordinate system, which was established by the plane of the maxillary tooth cusps. Because the principal components of the maxillary and mandibular tooth cusps are in the same anatomical directions, a rotation matrix that reorients the mandibular tooth cusps within a cranial coordinate system along their principal components also aligns them with the maxillary tooth cusps. The prcomp function of the R stats package was applied to these coordinates in each frame and the loading matrix was converted to Euler angles and a method described by Slabaugh (1999) and a modified version of the rotationMatrixtoEP function of the linkR package in R (v1.1.1, Olsen, 2016; Olsen and Westneat, 2016).

## **Reconstructing Hyoid Rigid Body Kinematics**

Hyoid anteroposterior and superoinferior positions were measured as the value of the X and Y coordinate, respectively, of the tantalum marker implanted in the midline of the hyoid. Velocity in either direction was measured as the marker coordinate's time derivative using the splinefun function of the R stats package (R Core Team, 2017).

Measuring the length of muscles attaching to the hyoid required reconstructing hyoid rigid body kinematics. Operating under the assumption that the markers are rigidly fixed to that bone, the XMALab algorithm that produces the rigid body transformation matrices minimizes error among all markers within the same bone (Knörlein et al., 2016). However, the assumption of rigidity was violated in the hyoid of each animal because inter-marker distances were observed to vary regularly during feeding. Examining each animal post mortem revealed that markers had been extruded a small distance from the bone during healing. The standard deviation of in vivo hyoid inter-marker distances in Monkey K was comparable to that of the precision study; however, the same in vivo measurement in Monkey J was more than an order of magnitude larger than that of precision study (Table 2). Consequently, the reconstructed hyoid for Monkey J was observed to be abnormally rotated around its anteroposterior axis in the *in vivo* XROMM data. This finding prompted the development of an alternative method of generating a transformation matrix. Because the middle hyoid marker was either within (Monkey J) or immediately adjacent (Monkey K) to the hyoid bone, new rigid body transformation matrices were generated using the rotonto function of the Morpho package in R (v2.5.1, Schlager, 2017) that generated zero error for the middle hyoid marker and minimized error for the other two markers. The alternative reconstruction resolved the abnormal rotation about the anteroposterior axis.

## **Reconstruction of Muscle Length and Orientation**

Muscle length (d) was defined as the Euclidean distance between muscle attachment points, either from bone-to-bone (posterior mylohyoid, geniohyoid, stylohyoid), reconstructed attachment-to-marker (styloglossus),

bone-to-marker (genioglossus, hyoglossus, anterior digastric, posterior digastric), or marker-to-marker (palatoglossus). Anterior mylohyoid length was not measured in this study. Muscle orientation was defined in each coordinate system by modeling the muscle as a vector of length d (E1).

$$d = \sqrt{(x_2 - x_1)^2 + (y_2 - y_1)^2 + (z_2 - z_1)^2}$$
 (E1)

This method is limited in its ability to measure fascicle length in all muscles. The fascicles of genioglossus insert into a tendon at the mandibular symphysis and therefore whole muscle length was measured. The fibers of the anterior digastric are unipennate, permitting reconstruction of fiber length; however, the posterior belly is bipennate and only whole muscle belly lengths were calculated. Moreover, the accuracy of this method may suffer in muscles that exhibit curvature *post mortem*, including mylohyoid, styloglossus, and hyoglossus.

Muscle orientation was expressed using the relative magnitudes of the anteroposterior  $(\hat{i})$ , superoinferior  $(\hat{j})$ , and mediolateral  $(\hat{k})$  components of the vector within each coordinate system.

$$\hat{i} = x_2 - x_1 \tag{E2}$$

$$\hat{j} = y_2 - y_1 \tag{E3}$$

$$\hat{k} = z_2 - z_1 \tag{E4}$$

The origin and insertion were ordered so that positive values were oriented anteriorly, superiorly, and right at rest to reflect the signs of the coordinate systems. Muscle angles were calculated in the coronal (ZY), sagittal (XY), and axial planes (XZ).

$$\theta_{\text{axial}} = \tan^{-1} \frac{\hat{i}}{\hat{k}} \tag{E5}$$

$$\theta_{\text{coronal}} = \tan^{-1} \frac{\hat{j}}{\hat{k}}$$
 (E6)

$$\theta_{\text{sagittal}} = \tan^{-1} \frac{\hat{j}}{\hat{i}}$$
 (E7)

The orientation of lines of action for each plane are demonstrated in Figure 5. In the axial plane, 0 degrees was right and 90 degrees was anterior. In the coronal plane, 0 degrees was right and 90 degrees was superior. In the sagittal plane, 0 degrees was anterior and 90 degrees was superior. Muscle linear and angular velocity were calculated by taking the first derivative of the data using the splinefun function of the R stats package (R Core Team, 2017).

## **Precision Study**

Precision experiments (following Menegaz et al., 2015) were conducted prior to specimen staining to evaluate whether the described methods are precise enough to measure *in vivo* muscle linear and angular displacement and velocity. In brief, the frozen specimen was waved within the

capture volume while running each X-ray emitter at the same voltage and current that was used in vivo and using the same camera frame rate and shutter speed. Five hundred frames were digitized to generate XYZ coordinates and rigid body transformations using XMALab (Knörlein et al., 2016). To characterize typical in vivo digitizing, markers were digitized using a combination of manual and automated digitizing; the refinement functions of XMALab were not used. The precision measurements were therefore more conservative (less precise) than if more time were put into digitizing. Muscle and tendon length, angle, velocity, and orientation were reconstructed from data collected during the precision study described above and the landmark-based definition of the coordinate system. Because the specimens were frozen and therefore the markers could not move relative to one another, three standard deviations of the various post mortem kinematic measurements were used to define a 99.7% confidence interval for in vivo measurements.

#### In Vivo Data Analysis

Muscle kinematics and strain were reconstructed from in vivo data in one of the animals (Monkey J) to determine whether the workflow is precise enough to study linear and angular displacement and velocity in the primate hyolingual apparatus. Swallow (N = 24) and chew (N=39) cycles defined from maximum gape to maximum gape were included in the analysis. The swallows digitized in this study were intercalated between chewing cycles although they do not come at the end of the sequence, these types of swallows have been shown to be fundamentally similar to human swallowing kinematics reported in the literature (Nakamura et al., 2017). Gape cycle phases (fast close, slow close, slow open, fast open) were determined by analyzing the acceleration of mandibular pitch using a modified version of the method described by Reed and Ross (2010) with the addition of an intercuspal phase (Palmer et al., 1992; Hiiemae et al., 1995) (Fig. 6). This intercuspal phase was defined by negative mandibular pitch, which indicated that the plane defined by the mandibular molar cusps had either intersected or elevated above that of the cranium. Chewing and swallowing in the animal had a frequency of 2-3 Hz, and the coordinates and rigid body transformations were low-pass filtered at 20 Hz using XMALab's filtering functions.

Muscle length and velocity were normalized by lengths observed *in vivo* by taking the average length reconstructed from 30 to 50 frames (150–250 ms) while structures of interest were not moving. Longer durations were not possible because the animals either frequently moved or were not still in postures that allowed digitization of the necessary markers. For each cycle, the range of each kinematic variable was calculated and the mean range was compared against the precision study results.

## **Sensitivity Analysis**

Posterior mylohyoid was found to exhibit a large *in vivo* range of all of the measured kinematic variables and was therefore used to investigate the extent to which using inaccurate or imprecise muscle attachment sites affects kinematic measurements. Four false attachment points on the mandible's surface were reconstructed 3.37 to 4.11 mm anterior, inferior, posterior, and superior to the actual attachment point (Fig. 7). The

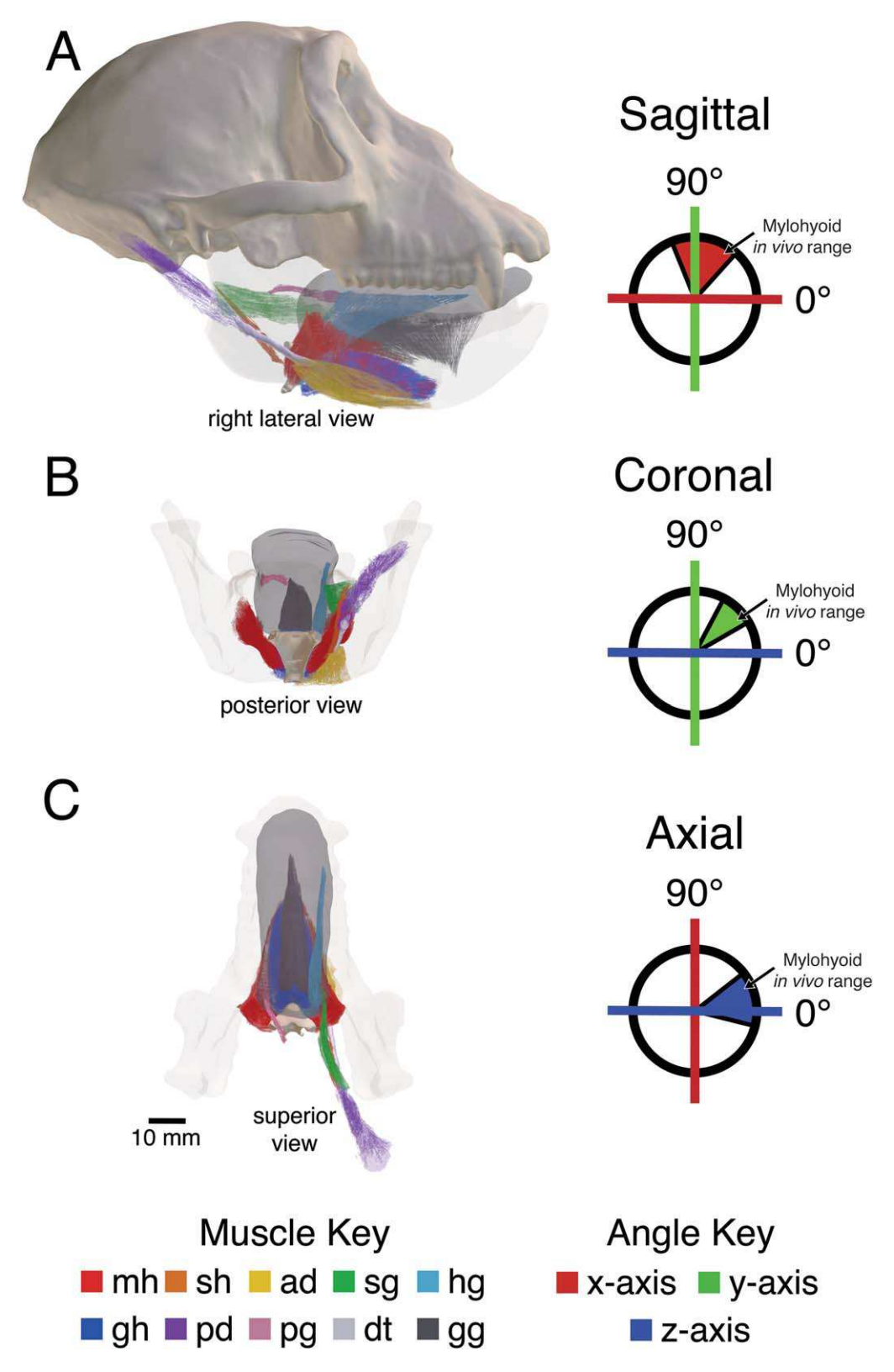


Fig. 5. Muscle orientation in anatomical planes. (A) Sagittal plane, right view. On the crosshair, the anteroposterior axis is red and superoinferior axis is green. Anterior is set at 0 and superior is set at 90. (B) Coronal plane, posterior view. On the crosshair, the mediolateral axis is blue and superoinferior axis is green. Right is set at 0 and superior is set at 90. (C) Axial plane, superior view. On the crosshair, the mediolateral axis is blue and anteroposterior axis is red. Right is set at 0, anterior is set at 90. Each crosshair's colored area indicates the posterior mylohyoid's *in vivo* range within a given plane in both cranial and mandibular coordinate systems. Abbreviations: ad, anterior digastric; gg, genioglossus; gh, geniohyoid; hg, hyoglossus; mh, mylohyoid; pd, posterior digastric; pg, palatoglossus; sg, styloglossus; sh, stylohyoid.

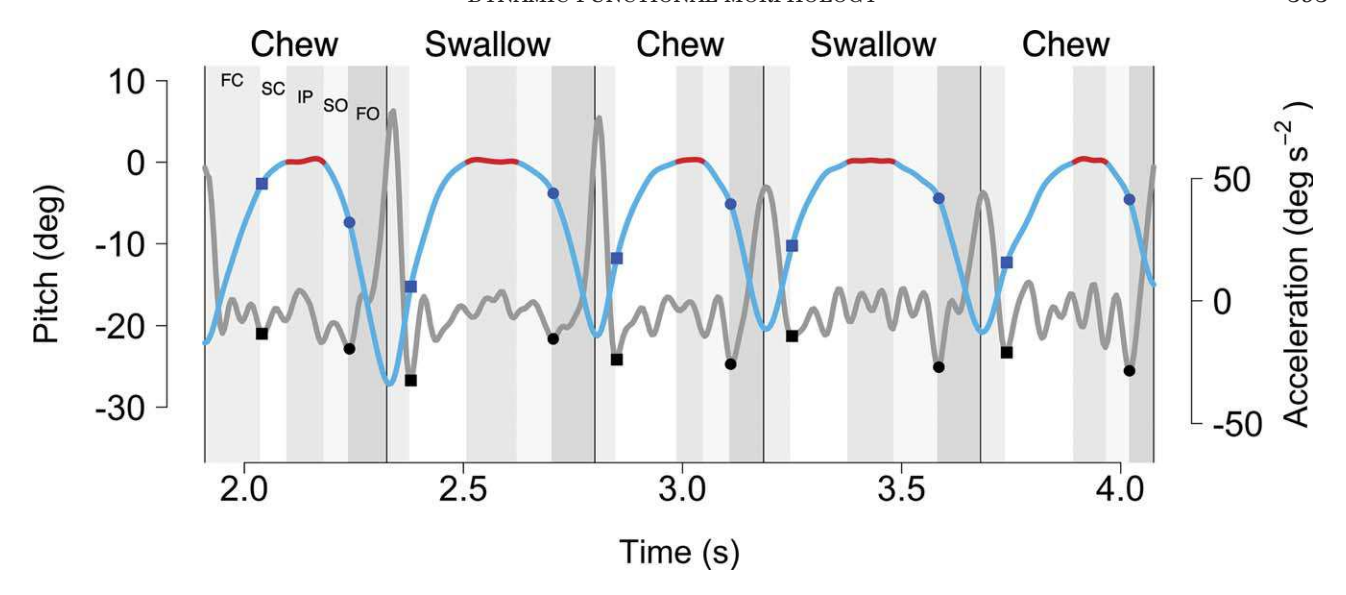


Fig. 6. Mandibular kinematics and gape cycle phases. Cycles are separated by black lines. Different colored gray boxes indicate different phase cycles indicated in the first cycle (FC, fast close; SC, slow close; IP, intercuspal phase; SO, slow open; FO, fast open). Light blue lines indicate mandible pitch, gray lines indicate mandible acceleration. Squares indicate the lowest acceleration prior to the intercuspal phase and indicate the FC-SC transition. Circles indicate the lowest acceleration after the intercuspal phase and indicate the SO-FO transition. The intercuspal phase is indicated on the pitch trace in red. Methods modified from Reed and Ross, 2010.

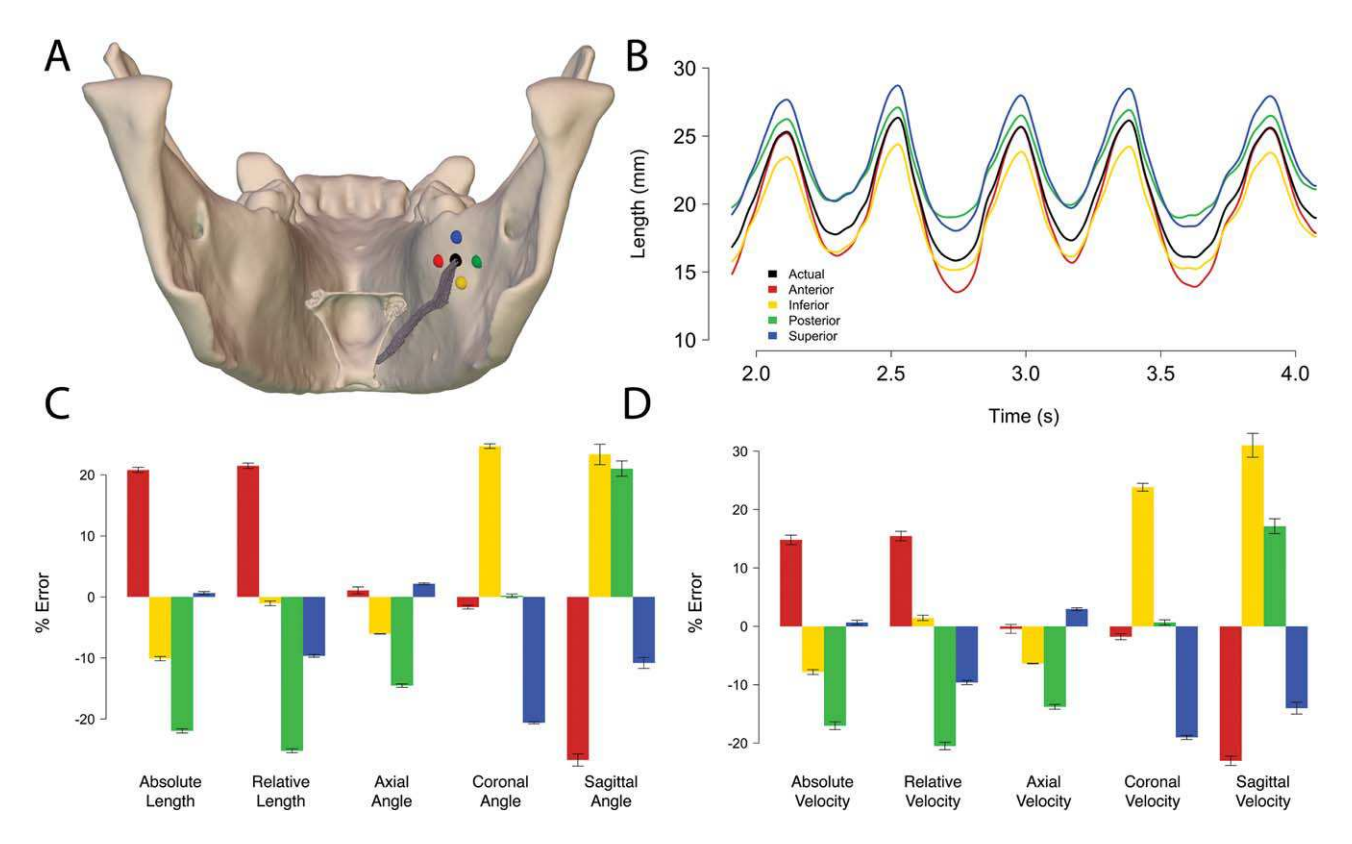


Fig. 7. Mylohyoid length using actual and estimated mandibular insertion points. (A) Mandible, basihyoid, and mylohyoid fascicle (gray) in posterior view. The locations of the various attachment points are shown as colored spheres. The black sphere is the actual insertion location, while the following colors have been displaced as follows: anteriorly, red; inferiorly, yellow; posteriorly, green; superiorly, blue. (B) Mylohyoid length during a feeding sequence. The colored lines correspond to the same color attachment site in A. Both the absolute value and range of mylohyoid length vary among the different attachment sites. (C) Error in the range of length measurements based on each false attachment location compared to the measurements based on the actual attachment location.

**TABLE 3. Registration error** 

	Mean intermarker distance (mm)									
		red using ific matrix		red using matrix						
Bone	Monkey J	Monkey K	Monkey J	Monkey K						
Cranium Mandible Hyoid All Markers	0.07 0.06 0.11 0.08	0.07 0.09 0.05 0.07	2.20 2.32 2.26	1.85 2.22 2.03						

range of each variable (Var) was obtained for each cycle and was then averaged across all cycles for the true and false attachment points. Percent error was calculated as:

$$Error = \frac{Var_{True} - Var_{False}}{Var_{True}} \times 100$$
 (E8)

#### RESULTS

### **Accuracy and Precision**

The average registration error of diceCT and unstained CT data sets using bone-specific transformation matrices was 0.08 mm (Table 3). These results indicate that the iodine staining protocol did not result in significant bone shrinkage. In contrast, staining deformed the soft tissues and moved the bones relative to one another; as a result, applying the cranial registration transformation matrix to the mandible and the hyoid introduced an average alignment error of 2.15 mm. Therefore, applying bone-specific transformation matrices is more accurate than applying a single transformation matrix to all bones and muscle models.

All *in vivo* kinematic ranges were greater than the precision of the system ( $\pm$  3 SD), and most (80%) were at least an order of magnitude greater (Tables 4 and 5). The mean precision of absolute linear velocity, normalized linear velocity, and angular velocity among all muscles was 7.58 mm s<sup>-1</sup>, 0.278 lengths s<sup>-1</sup>, and 29.8 deg s<sup>-1</sup>, respectively. Overall, the results indicate that the precision of both displacement and velocity are sufficient for kinematic analysis, but given the variability in precision, measurement- and muscle-specific precision values should be used.

## **Sensitivity Analysis**

Relatively small inaccuracies in muscle attachment location introduce significant error into most kinematic measurements (Fig. 7, Table 6). Averaging across chewing and swallowing cycles, measurements made from false muscle attachment sites differed from those of the actual attachment site by an average of 13.2% (range: 0.1% to 49.8%). Even if the range approximated the actual measurements, the absolute value was nonetheless different, as in the case of the superiorly displaced landmark and absolute length measurements.

## **Case Study of Hyoid Elevation**

The described method was applied to the functional morphology of the digastric, hyoglossus, posterior mylohyoid, and stylohyoid muscles, and the mechanism of

TABLE 4. Precision compared to in vivo range of muscle linear and angular displacement

								8				
		Muscle L	Muscle Linear Displacemen	lacement				Mu	Muscle Angular	Displaceme	ent	
		Absolute (m	(mm)	Normalized (	ed (L <sub>r</sub> )		Sagittal	(deg)	Coronal (deg)	(deg)	Axial (deg)	leg)
Muscle	Resting Length (mm)	$\begin{array}{c} \text{Precision} \\ (\pm 3 \text{ SD}) \end{array}$	In vivo range (mean)	$\begin{array}{c} \text{Precision} \\ (\pm 3 \text{ SD}) \end{array}$	In vivo range (mean)	Coordinate System	$\begin{array}{c} \textbf{Precision} \\ (\pm 3 \ \text{SD}) \end{array}$	In vivo range (mean)	Precision (±3 SD)	In vivo range (mean)	$\begin{array}{c} \text{Precision} \\ (\pm 3 \text{ SD}) \end{array}$	In viv range (mean
Anterior Digastric	24.09	0.09	4.59	0.004	0.190	Mandible	0.370	21.308	1.641	60.613	0.400	2.85
Digastric Tendon	18.07	0.12	0.83	900.0	0.046	Cranium	0.412	14.119	0.877	9.691	0.591	5.47
Genioglossus	19.81	0.12	7.72	900.0	0.390	Mandible	0.352	28.168	0.593	11.796	0.757	14.72
Geniohyoid	40.34	0.08	10.14	0.002	0.252	Mandible	0.188	15.401	1.676	140.956	0.178	2.44
Hyoglossus	52.73	0.15	11.46	0.003	0.218	Mandible	0.264	10.281	0.448	12.446	0.380	10.33
Mylohyoid	22.34	0.14	8.75	0.006	0.395	Mandible	0.266	33.999	0.422	20.816	0.298	39.68
Palatoglossus	11.31	0.11	3.22	0.010	0.285	Mandible	0.793	28.542	2.638	153.491	1.054	16.79
Posterior Digastric	41.29	0.21	1.92	0.005	0.046	Cranium	0.134	6.867	0.249	5.462	0.280	2.99
Styloglossus	38.22	0.12	7.74	0.003	0.203	Cranium	0.225	15.773	0.814	38.285	0.430	4.71
Stylohyoid	52.61	0.21	3.04	0.004	0.058	Cranium	0.209	10.462	0.197	4.963	0.329	5.42

TABLE 5. Precision compared to in vivo range of muscle linear and angular velocity

		Muscle line	ear velocity					Muscle ang	ular velocity		
	Absolute (	(mm s <sup>-1</sup> )	Norma (L <sub>r</sub> s			Sagittal (	deg s <sup>-1</sup> )	Coronal	$(\text{deg s}^{-1})$	Axial (d	eg s <sup>-1</sup> )
Muscle	Precision (±3 SD)	In vivo range (mean)	Precision (±3 SD)	In vivo range (mean)	Coordinate System	Precision (±3 SD)	In vivo range (mean)	Precision (±3 SD)	In vivo range (mean)	Precision (±3 SD)	In vivo range (mean)
Anterior Digastric	5.30	102.25	0.220	4.246	Mandible	20.087	410.929	89.935	2,216.655	22.273	96.849
Digastric Tendon	6.81	31.52	0.377	1.744	Cranium	20.980	347.644	49.574	274.954	34.080	146.105
Genioglossus	5.92	241.16	0.299	12.176	Mandible	19.848	637.669	30.917	341.581	39.691	558.814
Geniohyoid	5.15	192.38	0.121	4.786	Mandible	10.367	294.361	95.921	7,223.758	10.024	72.920
Hyoglossus	7.80	295.60	0.148	5.621	Mandible	15.130	352.740	21.712	347.102	18.173	306.501
Mylohyoid	8.00	177.79	0.361	8.017	Mandible	16.080	729.132	22.369	381.114	18.571	783.111
Palatoglossus	6.32	108.89	0.559	9.632	Mandible	41.829	775.336	151.564	7,685.765	55.633	486.575
Posterior Digastric	12.04	66.05	0.292	1.600	Cranium	9.377	169.667	13.498	121.622	17.703	82.880
Styloglossus	7.08	183.59	0.185	4.803	Cranium	12.611	415.984	38.379	1,196.357	20.973	143.891
Stylohyoid	11.20	85.49	0.213	1.629	Cranium	13.258	251.978	9.219	125.986	17.720	150.956

TABLE 6. Mean range of mylohyoid kinematics measured using actual and displaced mandibular insertion points

		Mean range of	mylohyoid li	inear kinematics		Mean range of mylohyoid rotational kinematics							
	Resting	Absolute (m	m s <sup>-1</sup> )	Normalized	$(L_r s^{-1})$		Sagittal	$(\text{deg s}^{-1})$	Coronal	$\log s^{-1}$	Axial	$(\text{deg s}^{-1})$	
Insertion Location	Length (mm)	Displacement	Linear Velocity	Displacement	Linear Velocity	Coordinate System	Angle	Angular Velocity	Angle	Angular Velocity	Angle	Angular Velocity	
Actual Anterior Inferior Posterior Superior	22.34 22.24 20.30 23.28 24.87	8.75 10.58 7.86 6.83 8.81	177.79 203.43 164.02 148.06 179.04	0.395 0.480 0.390 0.295 0.357	8.017 9.225 8.140 6.397 7.249	Mandible Mandible Mandible Mandible Mandible	33.999 25.284 42.665 40.632 29.937	729.132 562.852 967.020 848.157 620.890	20.816 20.506 25.928 20.819 16.521	381.114 374.187 472.027 383.693 308.443	39.687 40.251 37.288 33.866 40.507	783.111 778.626 732.984 674.868 806.427	

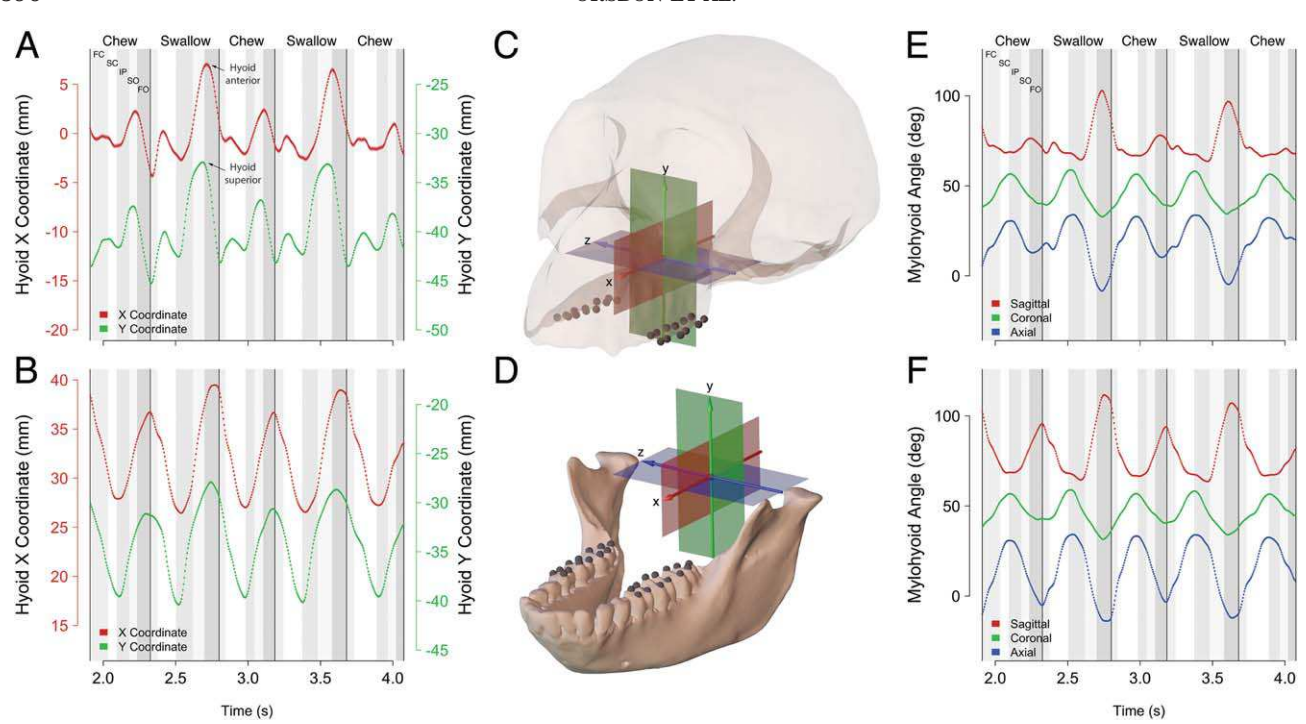


Fig. 8. Mylohyoid rotation in different coordinate systems. (A) Hyoid anteroposterior (red, larger values are anterior) and superoinferior (green, larger values are superior) kinematics in a cranial coordinate system. Gray bars indicate gape cycle phases (FC, fast close; SC, slow close; IP, intercuspal phase; SO, slow open; FO, fast open). (B) Hyoid kinematics in a mandibular coordinate system using the same conventions as A. (C) Cranial coordinate system with the origin on the posterior nasal spine. (D) Mandibular coordinate system with the origin halfway between the most medial points of the mandibular condyles. Red corresponds to the anteroposterior (X) axis and said plane, green to the superoinferior (Y) axis and coronal plane, and blue to the mediolateral (Z) axis and axial plane, with all arrows pointing in the positive direction. The location of the maxillary and mandibular molar cusps are shown as gray spheres. (E) Mylohyoid rotation in a cranial coordinate system. (F) Mylohyoid rotation in a mandibular coordinate system. See Figure 5 for how these angles are oriented in each plane. Faded lines for kinematic variables indicate a 99.7% confidence interval (3 SD) based on precision study results for each variable.

hyoid elevation in chewing versus swallowing. The following is a qualitative analysis of observations from the case study; future work will further delve into these phenomena quantitatively.

Figure 8 illustrates data from a representative sequence of five successive chewing (N = 3) and swallowing (N=2) cycles and demonstrates the importance of the choice of coordinate system when quantifying muscuoloskeletal kinematics and relating them to muscle function. In a cranial coordinate system, posterior mylohyoid and hyoid exhibit more complex and larger amplitude movements in chewing than swallowing. However, in a mandibular coordinate system, posterior mylohyoid and hyoid kinematics are more sinusoidal and similar between chews and swallows, although amplitudes are still greater in swallows. Therefore, the complex kinematics observed in a cranial coordinate system are the product of two much simpler movements (mandibular movement relative to the cranium and hyoid movement relative to the mandible), and slight modification in the timing and amplitude of these two movements underlies the observed difference between chewing and swallowing. Additionally, when the hyoid is in more posterior and inferior positions within the cranial coordinate system at maximum gape (indicated by black vertical lines),

the hyoid is nearly at its most anterior and superior position relative to the mandible. These distinctions are relevant when considering muscle function because they implicate both hyoid depressors (e.g., sternohyoid) and elevators (e.g., mylohyoid) in determining hyoid posture at maximum gape.

Because most of the potential hyoid elevators either attach directly to the mandible (posterior mylohyoid, anterior digastric) or are influenced by mandibular movements (i.e., hyoglossus via the tongue), subsequent analyses are reported in a mandibular coordinate system.

In chews, there is a tight relationship between hyoid elevation and posterior mylohyoid length (Fig. 9); however, in swallows the amplitude of hyoid kinematics exceeds changes in mylohyoid length and velocity, demonstrating that hyoid kinematics exhibit some decoupling from mylohyoid fiber length. In swallows, the posterior mylohyoid achieves most of its shortening by late slow opening (SO), yet the hyoid continues to elevate until early-to-mid fast opening (FO). From late SO to early-to-mid FO, the posterior mylohyoid continues to rotate in the coronal and sagittal planes (Fig. 8), suggesting that fiber rotation may account for the continued movement of the hyoid despite a lack of change in posterior mylohyoid length.

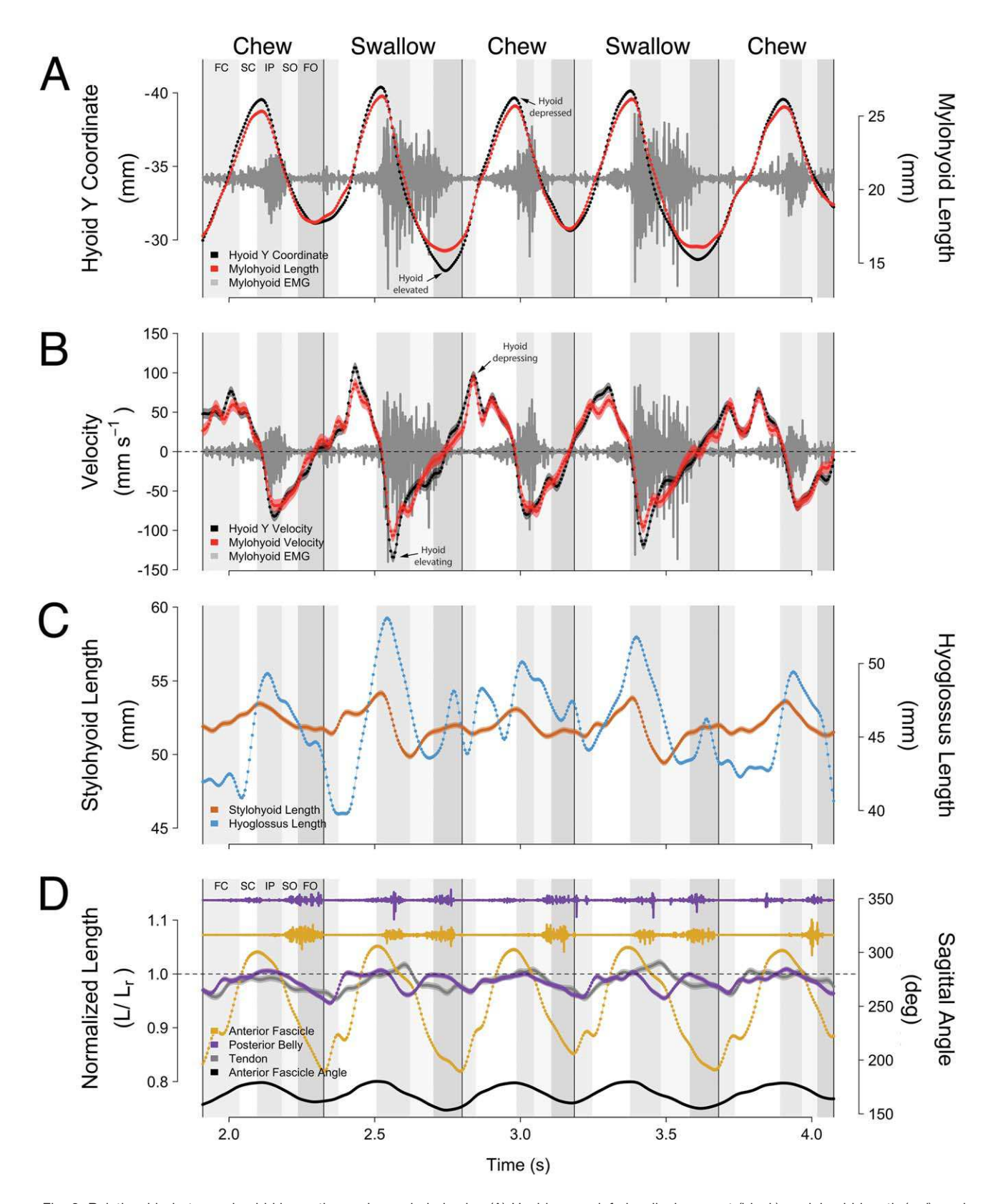


Fig. 9. Relationship between hyoid kinematics and muscle behavior. (A) Hyoid superoinferior displacement (black), mylohyoid length (red), and mylohyoid EMG (gray). (B) Hyoid superoinferior velocity (black), mylohyoid velocity (red), and mylohyoid EMG (gray). The dashed line indicates zero velocity. (C) Hyoglossus length (light blue) and stylohyoid length (orange). (D) Anterior (yellow) and posterior (purple) digastric muscle and tendon (gray) normalized length during the same feeding sequence. The dashed line indicates the muscles' resting length. Electrography data for the anterior and posterior digastric are shown as solid yellow and purple lines, respectively. Anterior digastric fascicle sagittal angle is shown in black; smaller values indicate a more superior orientation. Cycles are defined from maximum gape to maximum gape. Faded lines for kinematic variables indicate a 99.7% confidence interval (3 SD) based on precision study results for each variable. Background gray bars indicate different phases of the gape cycle using the same convention as Figure 6. All measurements are taken in a mandibular coordinate system.

Posterior mylohyoid was most active while shortening in both chewing and swallowing. However, in many cycles there is low-level activity during the late stages of muscle lengthening immediately prior to shortening. Posterior mylohyoid activity during chewing is limited primarily to late slow closing (SC), intercuspal phase (IP), and SO phases of the jaw cycle. In contrast, posterior mylohyoid exhibits higher amplitude activity in swallowing and extended from late SC through early FO, indicating a fundamental difference in both motor unit recruitment magnitude and timing relative to jaw movements in swallowing as compared to chews. These changes in timing likely contribute in the previously discussed differences in hyoid movements relative to the cranium. Correspondingly, posterior mylohyoid shortening and hvoid elevation displacement and velocity are greater during IP in swallows than in chews. Given that the posterior mylohyoid shortens further, shortens faster, and rotates more in swallowing than in chews, the greater activity of the posterior mylohyoid may enhance hyoid elevation velocity and displacement more than it enhances superiorly oriented force (Azizi et al., 2008). However, loss in force due to increased shortening velocity may be offset by the recruitment of more motor units.

Before concluding that active fiber rotation functionally contributes to hyoid kinematics during swallowing, active shortening in potential synergists must be ruled out. In the sagittal plane, stylohyoid is superiorly and posteriorly oriented (range: 122.4-149.2 degrees, anterior = 0 degrees, superior = 90.0 degrees) while hyoglossus is superiorly and anteriorly oriented (range: 30.5-54.5 degrees). During swallowing, the stylohyoid lengthens throughout jaw opening phases while hyoglossus lengthens from mid-to-late SO to mid FO. Therefore, neither of these muscles' shortening could account for the continued elevation of the hyoid relative to the mandible from mid SO to mid FO. However, both muscles shorten during IP and may contribute to the observed increased hyoid elevation velocity relative to mylohyoid shortening velocity.

Functional differences between chews and swallows are also evident in the digastric. Both bellies exhibit activity during jaw opening, and in swallows the anterior digastric features an additional burst during IP. Posterior digastric firing patterns are similar in chews and swallows, with greater activity during IP in swallows. However, this channel may be contaminated by crosstalk with the nearby medial pterygoid. The main difference between chews and swallows is evident during IP in swallows, when the anterior and posterior digastric shorten more than in chews, and the digastric tendon lengthens beyond its resting length. The observed digastric tendon strain decouples fiber length from whole muscle length. In contrast, the tendon changes relatively in phase with changes in posterior digastric length in chews. Afterward, the tendon rapidly shortens as the posterior digastric lengthens and the anterior digastric continues to shorten. Additionally, the anterior digastric rotates throughout chewing and swallowing cycles (range: 152.6-181.1 degrees, superior = 90.0 degrees, posterior = 180.0 degrees), reaching its most superior orientation in FO during swallowing.

## **DISCUSSION**

We demonstrate a method of integrating highresolution muscle imaging (diceCT, Gignac et al., 2016) with marker-based XROMM (Brainerd et al., 2010), fluoromicrometry (FMM, Camp et al., 2016), and EMG to improve the accuracy of muscle length and velocity measurements synchronized with muscle activity. The precision of the method is sufficient to study the kinematics of the macaque hyoid and hyoid musculature, including both linear and angular velocity. The methods described are particularly useful for musculoskeletal systems like the primate hyolingual apparatus where multiple muscles underlie movements that cannot be observed using standard reflected-light motion capture technology.

## **Hyolingual Functional Morphology**

The lines of action of many hyolingual muscles are not parallel to the sagittal plane; consequently, the functional morphology of the hyolingual apparatus must be studied in three dimensions (German et al., 2011). Our preliminary findings corroborate prior 2D work that found similarities between chewing and swallowing hyoid kinematics in a mandibular but not cranial coordinate system (Palmer et al., 1992; Hiiemae and Palmer, 1999). Similarly, patterns of mylohyoid muscle length changes between chewing and swallowing are also fundamentally similar despite differences in patterns of activity. In contrast, different patterns of digastric activity may underlie the decoupling of muscle belly and tendon length observed in swallowing.

These preliminary results corroborate a human study in which muscle length dynamics alone were insufficient to explain the observed hyoid kinematics (Okada et al., 2013). The macaque posterior mylohyoid continues rotating after it ceases to change length, and our results indicate that this rotation cannot be explained by continued shortening of the stylohyoid or hyoglossus. Enhanced hyoid elevation velocity during swallowing IP may be due to active shortening of the stylohyoid and hyoglossus; however, analysis of these muscle's EMG signals is hampered by cross-talk resulting from their proximity to other muscles in the tightly-packed space between the mandibular rami. Continued hyoid elevation could be due to continued shortening of the anterior digastric; however, considering that the anterior digastric is oriented primarily anteroposteriorly, its contributions to hyoid elevation (if any) are also likely to be due to fiber rotation that occurs as active muscle shortening takes up slack and linearizes the three segments. Previous in vitro work has demonstrated that increased fiber rotation increases the velocity of whole muscle kinematics but reduces force along the line of action (Azizi et al., 2008). Therefore, given that the fascicles of key hyoid elevators rotate as well as shorten, increased muscle activity during swallowing may contribute to swallowing performance by generating higher hyoid elevation velocities rather than higher superiorly-oriented forces. Human studies demonstrating slower hyoid velocities among individuals with dysphagia further supports the importance of velocity in hyolingual performance during swallowing (Wang et al., 2010; Seo et al., 2016).

The absence of activity in the anterior digastric during its initial shortening during IP in chewing was unexpected given that maximum digastric force is produced at or near minimum gape in several species of non-primate mammals (Mackenna and Türker, 1978; Muhl,

1982; Anapol et al., 1987; Anapol and Herring, 1989). However, the EMG activity of the anterior digastric, including the differences in behavior between chewing and swallowing, is very similar to that described by Hylander and colleagues (1987). For the sake of argument, let us assume that the whole-fiber length-tension curve of the primate anterior digastric does not differ from other mammals. Given that optimal fiber length is plastic and increases in response to either active or prolonged passive stretch (Williams and Goldspink, 1973; Butterfield et al., 2005), the anterior digastric's activity near its assumed optimal length during swallowing but not chewing suggests that the fiber's optimal length is determined by either swallowing performance requirements or the fact that a low gape angle also happens to be its resting position. Being on the optimal part of the length-tension curve during IP of intercalated swallowing may mitigate the losses in force that are presumably incurred through active anterior digastric rotation (Azizi et al., 2008). Developing tension in a superiorly rotating anterior digastric along with the anterior mylohyoid may facilitate the high hyoid elevation velocities during IP by supporting the mass of the tongue, relieving the posterior mylohyoid of gravitational loading that would result in higher muscle force production but lower velocity for a given level of activation.

Notably, in chewing, the anterior digastric shortens during IP and early SO without being active. Given that the anterior digastric is longer than its resting length during IP in chewing, shortening may also be due to passive tension developed during SC. In the absence of such passive forces, posterior mylohyoid active shortening (in addition to geniohyoid, not shown) may be responsible for the earlier, slower phases of jaw opening that occur simultaneously with hyolingual elevation and protrusion while the digastrics contribute to the later, faster phases. However, such functional conclusions require additional data about activity in the lateral pterygoids.

The behavior of the anterior digastric suggested here highlights the importance of integrating multiple lines of evidence across multiple organismal behaviors when inferring musculoskeletal design. One can calculate the length-tension curve physiologically by experimentation or morphologically by relating fiber length to sarcomere length (Winters et al., 2011), but neither approach reveals that the anterior digastric may actively produce force closer to the optimal part of its length-tension curve during swallowing than during chewing.

Replication in more individuals is necessary to support the generalizability of the observed fascicle kinematics (including rotation), eccentric activity, muscletendon dynamics, and behavior-specific muscle activation patterns and to assess their contributions to feeding performance. These findings, though consistent with other findings in the literature, may not apply to all rhesus macaques, let alone all non-human primates. Future work (currently underway) will compare similar metrics among at least four rhesus macaques (two male, two female), including the two used in this study. Expansion to additional primate species as well as non-primate mammals and non-mammalian tetrapods would provide an essential comparative dataset for experimentally investigating functional the morphology

comparative biomechanics of the mammalian hyolingual apparatus and clade-specific behaviors, e.g., suckling.

## Advantages

The integration of XROMM, FMM, diceCT, and EMG brings high accuracy and precision to the study of muscles that are difficult to access surgically for FMM alone. Anatomical considerations can limit the muscles accessible for *in vivo* study, and expanding beyond the more easily accessible muscles is necessary to broaden our understanding of how variability in musculoskeletal form relates to variability in function and performance. *In vivo* application of the described method can be used to validate similar *in silico* approaches to understanding muscle function and coordination among behaviors.

The described method is a robust means of determining muscle attachment site location for in vivo kinematics. The registration process is highly accurate (mean error = 0.08 mm), and using the actual site of attachment rather than relying on bony landmarks will reduce errors introduced by manually assigning muscle attachment site location. Despite the fact that precision decreases when taking the time derivative of displacement, the method's precision is high enough to measure velocity in this musculoskeletal system. To our knowledge, this study is the first to demonstrate the precision of absolute linear, relative linear, and angular velocity measurements using XROMM or fluoromicrometry (mean =  $7.58~\mathrm{mm~s^{-1}}$ ,  $0.278~\mathrm{lengths~s^{-1}}$ , and  $29.8~\mathrm{deg~s^{-1}}$ , respectively). The precision reported here is a conservative (i.e., worse precision) estimate, given that the refinement features of XMALab were not used. Precision could be improved by using these refinement features or by utilizing higher magnification settings on the X-ray machinery for smaller organisms. However, the described methods are not necessarily appropriate for different organisms with faster behaviors because velocity precision is also inversely related to frame rate. Nonetheless, if the velocity of behavior increases proportionally to the increases in system noise—i.e., if the signal-to-noise ratio remains constant—then higher frame rates should pose no analytical problems. Ideally, precision tests should be conducted for each study organism and equipment specifications to determine if the experimental design is sensitive enough for the behaviors of interest (Menegaz et al., 2015).

Skeletal kinematics from XROMM and soft tissue kinematics from FMM are measured within the same coordinate system and are therefore readily related to one another. A key advantage of XROMM and FMM is that they allow wireless data collection (Camp et al., 2016), which facilitates measuring multiple muscles simultaneously. Although similar measurements of bony kinematics can be obtained using traditional reflected-light motion capture methods (e.g., Reed and Ross, 2010; Ross et al., 2012), and whole muscle kinematics (length and moment arm) can be calculated from kinematics of bone attachment points (e.g., Iriarte-Diaz et al., 2017), collecting simultaneous data on fascicle kinematics from multiple muscles remains a challenge for light-based approaches (Dick et al., 2016, 2017).

While the example described here involves in vivo data collection, Autodesk Maya's powerful animation capabilities and XROMM's user-friendly scripts could be

used for in silico modeling to evaluate how skeletal motion affects whole-muscle length, orientation, and moment arm, as has been performed with other modeling software (Hutchinson et al., 2005; Delp et al., 2007; Hutchinson et al., 2015; Charles et al., 2016b). Given that visible iodine staining is reversible by either leaching or soaking in sodium thiosulfate (Gignac et al., 2016; Morhardt et al., 2016), this method could be applied to museum specimens with intact soft tissue without damaging or destroying the specimens. Provided that validated methods of inferring joint kinematics from the morphology of the hard and soft tissues of the joint are used (e.g., Hammond et al., 2016), incorporating motion to the study of morphology of organisms that cannot be brought into the lab is an invaluable tool for testing musculoskeletal functional hypotheses in phylogenetic and ecological contexts (Lautenschlager, 2015). However, the limitations of tissue penetration by iodine mean that more expensive methods such as MRI, or destructive methods such as traditional PCSA techniques may still be necessary to measure pennation angle in larger specimens (Li et al., 2015, 2016). Moreover, measures of sarcomere length from muscles in known postures are still necessary for calculating whole muscle PCSA and length tension curves across joint excursions (Felder et al., 2005; Eng et al., 2009; Taylor and Vinyard, 2009; Winters et al., 2011). Therefore, tissue samples are required to normalize fiber length, but these could be limited to biopsies performed with specialized equipment (Ward et al., 2009b). While some degree of invasive sampling is still required to model a muscle's length-tension curve, in silico modeling may increase the morphological diversity accessible for functional morphology research. Nonetheless, such models should be validated by in vivo research where possible.

#### Limitations

The dependence of XROMM on X-ray imaging imposes several limitations. It requires access to either a dedicated XROMM facility or two C-arms outfitted with cameras of a sufficiently high frame rate for the behavior of interest. The behaviors that can be studied using XROMM are limited to those which can be executed within the capture volume, which depends on the size of the image intensifiers and magnification settings (Brainerd et al., 2010). Many intraoral feeding behaviors are compatible with XROMM, but locomotion poses significant challenges. For example, the organism may need to locomote on a treadmill or similar device within a constrained space, which may not fully recapitulate natural behavior. Combination of traditional reflected light motion capture with XROMM can ameliorate but not remove this constraint.

The dependence of diceCT on iodine or other postmortem staining means the animal must be sacrificed and scanned with a CT scanner with sufficient resolution to visualize fascicles of interest. If MRI is used for *in vivo* imaging of muscle instead, one could use diffusion weighted tensor imaging to trace muscle fascicles, provided sufficient resolution is attainable (Gilbert and Napadow, 2005; Gilbert et al., 2006; Taylor et al., 2015). However, even with these data on muscle volume and fascicle orientation, estimates of PCSA still require measures of sarcomere length in a fixed posture to normalize

fiber length (Anapol and Barry, 1996; Anapol and Gray, 2003; Anapol et al., 2004; Felder et al., 2005). Without these data, estimates of PCSA, and therefore muscle force, are fundamentally flawed.

The whole muscle and whole fiber lengths estimated using our method do not provide information on sarcomere length dynamics, which impairs our ability to estimate muscle force. Fascicles and sarcomeres exhibit strain heterogeneity, the functional consequences of which are unclear (Ahn et al., 2003; Konow et al., 2010; Wentzel et al., 2011; Holman et al., 2012; O'Connor et al., 2016; Moo et al., 2016). Muscle morphology may contribute to strain heterogeneity, as the more peripheral fibers in fusiform muscles may have different strain patterns than more central fibers (Pappas et al., 2002; Blemker et al., 2005; Zatsiorsky and Prilutsky, 2012). The extent to which non-uniform sarcomere lengths affect in vivo function and models of muscle kinetic dynamics or average out across the length of the muscle remains to be established. Additionally, some muscles, such as styloglossus, exhibit curvature of their long axis. Therefore, the Euclidean distance between attachment points is likely an inaccurate measure of muscle length for nonlinear muscles. Some authors have resolved this problem using muscle wrapping features in programs like OpenSIM (Hutchinson et al., 2005; Hutchinson et al., 2015; Charles et al., 2016a,b), and the development of similar scripts in Autodesk Maya would allow XROMM users to readily incorporate similar compensations to the XROMM workflow.

Although EMG data provide estimates of relative number of motor units and firing rates through time, its use in inferring the timing and magnitude of force production is currently limited. The timing of force onset and offset is delayed relative to EMG onset and offset, and the magnitude of these delays varies with muscle fiber type (Norman and Komi, 1979; Ross et al., 2005; Roberts and Gabaldón, 2008) and velocity (Cavanagh and Komi, 1979; Hylander and Johnson, 1989, 1993; Roberts and Gabaldón, 2008; Zatsiorsky and Prilutsky, 2012). As reviewed in the introduction, force magnitude is a dynamic product of activity level and fiber length, rotation, velocity, and history. Poorly understood interactions among all of these variables currently confound accurate predictions of dynamic muscle force when all of these variables are known, let alone when only activity is measured. Force can be more directly measured in individual muscles with tendons by buckle transducers (Barnes and Pinder, 1974) or fiber optic sensors (Komi et al., 1996); however, such methods cannot be applied to the many muscles with external tendons too short for these implants. The void in our knowledge about force production of multiple individual muscles may be filled in the future by in silico approaches such as inverse dynamics, in which individual muscle forces are predicted from kinematics, PCSA, and output forces such as ground reaction forces (Erdemir et al., 2007; Basafa et al., 2014; Russo et al., 2014). However, until kinetic predictions are validated by direct measurements of muscle force production, hypotheses generated by inverse dynamics models must still be interpreted with caution rather than confidence.

Lastly, XROMM and diceCT data are laborious to analyze because of the amount of time spent processing the data. The described method is excellent for studying

motion with high spatiotemporal resolution over a relatively small number of trials, but obtaining sufficient intra-individual sample sizes to compare musculoskeletal function across multiple behaviors and conditions currently poses a significant temporal challenge. This is particularly true for primate feeding-cycle-to-cycle differences account for a majority of the kinematic variation during mastication across species and food types, presumably due to changing bolus material properties over the course of the feeding sequence (Reed and Ross, 2010, 2012). Continued advances in semi- and fullyautomated marker tracking (Knörlein et al., 2016) are necessary for these methods to be practically applied to orders of magnitude more trials, as has been done for skeletal kinematics and whole muscle length change with Vicon (Reed and Ross, 2010; Ross et al., 2012; Iriarte-Diaz et al., 2017). Using more automated methods to segment fascicles from diceCT data sets may reduce post-scanning processing time and would make the segmentation step of this method more replicable (Kupczik et al., 2015; Dickinson et al., 2018). Such temporal challenges must be surmounted before these methods are a practical and efficient means of testing functional hypotheses in more depth, such as comparing muscle function across multiple behaviors and conditions, as well as with the taxonomic breadth necessary to robustly argue that a structure has emerged through natural selection to endow an organism with a functional adaptation.

## **CONCLUSIONS**

Musculoskeletal function is the product of tradeoffs and interactions among several biomechanical processes. Some of these processes, such as elasticity and variable gearing, decouple fiber length from muscle-tendon unit length and have frequently been ignored for the sake of simplifying morphological models. However, in vivo research suggests that these phenomena can be biomechanically significant. Techniques that capture many of the dynamic components of muscle can be used to test hypotheses about their contributions to organismal performance, to probe underlying assumptions about musculoskeletal functional morphology, and potentially to validate morphological correlates with dynamic processes that amplify force or velocity performance. Motion is an essential element of musculoskeletal design, and dynamic approaches continue to advance the field of musculoskeletal functional morphology. Application of these methods will help determine how organisms navigate the redundant routes of tuning power, force, and velocity in functional systems to improve ecologicallyrelevant performance through musculoskeletal design.

## **ACKNOWLEDGMENTS**

We thank Dr. Aaron Olsen for assistance with calculations and R scripting, Dr. Bhart-Anjan Bhullar and Dr. Ashley Morhardt for assistance with iodine staining protocols, Dr. Elizabeth Brainerd and Dr. Benjamin Knörlein for feedback on hyoid reconstructions, Carrie Anne Balcer for assistance with animal training and care, Dr. Kathryn Murray for creating the EMG connectors, April Isch-Neander for assistance with the microCT scanner, the veterinary and husbandry staff at the

University of Chicago for tirelessly keeping our animals healthy, and Dr. Adam Hartstone-Rose and two anonymous reviewers for feedback on the manuscript. This research was supported by the American Association of Anatomists Short Term Visiting Scholarship, the National Science Foundation (Major Research Instrumentation award DBI-1338066 and Doctoral Dissertation Research Improvement Grant BCS-1732175), and the National Institutes of Health (NIDCR R01-DE023816 and NICHD T32-HD009007).

#### LITERAUTRE CITED

Abbott BC, Aubert XM. 1952. The force exerted by active striated muscle during and after change of length. J Physiol 117:77–86.

Aerts P. 1998. Vertical jumping in Galago senegalensis: the quest for an obligate mechanical power amplifier. Phil Trans R Soc Lond B 353:1607–1620.

Ahn AN, Monti RJ, Biewener AA. 2003. In vivo and in vitro heterogeneity of segment length changes in the semimembranosus muscle of the toad. J Physiol 549:877–888.

Aiello BR, Blob RW, Butcher MT. 2013. Correlation of muscle function and bone strain in the hindlimb of the river cooter rurtle (Pseudemys concinna). J Morphol 274:1060–1069.

Aiello BR, King HM, Hale ME. 2014. Functional subdivision of fin protractor and retractor muscles underlies pelvic fin walking in the African lungfish (*Protopterus annectens*). J Exp Biol 217: 3474–3482.

Aiello BR, Westneat MW, Hale ME. 2017. Mechanosensation is evolutionarily tuned to locomotor mechanics. Proc Natl Acad Sci 114: 4459–4464.

Altringham JD, Ellerby DJ. 1999. Fish swimming: patterns in muscle function. J Exp 202:3397–3403.

Anapol FC, Muhl ZF, Fuller JH. 1987. The force-velocity relation of the rabbit digastric muscle. Arch Oral Biol 32:93–99.

Anapol FC, Herring SW. 1989. Length-tension relationships of masseter and digastric muscles of miniature swing during ontogeny. J Exp Biol 143:1–16.

Anapol FC, Barry K. 1996. Fiber architecture of the extensors of the hindlimb in semiterrestrial and arboreal guenons. Am J Phys Anthropol 99:429–447.

Anapol FC, Gray JP. 2003. Fiber architecture of the intrinsic muscles of the shoulder and arm in semiterrestrial and arboreal guenons. Am J Phys Anthropol 122:51–65.

Anapol FC, Shahnoor N, Gray JP. 2004. Fiber architecture, muscle function, and behavior: Gluteal and hamstring muscles of semi-terrestrial and arboreal guenons. In: Anapol FC, German RZ, Jablonski N, editors. Shaping primate evolution. Cambridge: Cambridge University Press.

Anderson CV. 2016. Off like a shot: Scaling of ballistic tongue projection reveals extremely high performance in small chameleons. Sci Rep 6:18625.

Anderson CV, Deban SM. 2010. Ballistic tongue projection in chameleons maintains high performance at low temperature. Proc Natl Acad Sci USA 107:5495–5499.

Arnold EM, Hamner SR, Seth A, Millard M, Delp SL. 2013. How muscle fiber lengths and velocities affect muscle force generation as humans walk and run at different speeds. J Exp Biol 216: 2150–2160.

Astley HC, Roberts TJ. 2012. Evidence for a vertebrate catapult: Elastic energy storage in the plantaris tendon during frog jumping. Bio Lett 8:386–389.

Astley HC, Roberts TJ. 2014. The mechanics of elastic loading and recoil in anuran jumping. J Exp Biol 217:4372–4378.

Azizi E, Brainerd EL, Roberts TJ. 2008. Variable gearing in pennate muscles. Proc Natl Acad Sci USA 105:1745–1750.

Azizi E, Roberts TJ. 2014. Geared up to stretch: Pennate muscle behavior during active lengthening. J Exp Biol 217:376–381.

Barnes GRG, Pinder DN. 1974. *In vivo* tendon tension and bone strain measurement and correlation. J Biomech 7:35–42.

- Basafa E, Murphy RJ, Gordon CR, Armand M. 2014. Modeling the biomechanics of swine mastication - An inverse dynamics approach. J Biomech 47:2626–2632.
- Bernstein N. 1967. The co-ordination and regulation of movements. 1st English ed. Oxford NY: Pergamon Press.
- Biewener AA. 1989. Scaling body support in mammals: Limb posture and muscle mechanics. Science 245:45–48.
- Biewener AA. 1990. Biomechanics of mammalian terrestrial locomotion. Science 250:1097–1103.
- Biewener AA. 1992. Biomechanics—Structures and systems: A practical approach. Oxford: Oxford University Press.
- Biewener AA. 1998. Muscle function *in vivo*: A comparison of muscles used for elastic energy savings versus muscles used to generate mechanical power. Am Zool 38:703–717.
- Biewener AA, Corning WR, Tobalske BW. 1998. *In vivo* pectoralis muscle force-length behavior during level flight in pigeons (*Columba livia*). J Exp Biol 201:3293–3307.
- Biewener AA, Konieczynski DD, Baudinette RV. 1998. *In vivo* muscle force-length behavior during steady-speed hopping in tammar wallabies. J Exp Biol 201:1681–1694.
- Biewener AA, Farley CT, Roberts TJ, Temaner M. 2004. Muscle mecahnical advantage of human walking and running: Implications for energy cost. J Appl Physiol 97:2266–2274.
- Blemker SS, Pinsky PM, Delp SL. 2005. A 3D model of muscle reveals the causes of nonuniform strains in the biceps brachii. J Biomech 38:657–665.
- Brainerd EL, Baier DB, Gatesy SM, Hedrick TL, Metzger KA, Gilbert SL, Crisco JJ. 2010. X-Ray Reconstruction of Moving Morphology (XROMM): Precision, accuracy and applications in comparative biomechanics research. J Exp Zool Part A 313:262–279.
- Butterfield TA, Leonard TR, Herzog W. 2005. Differential serial sarcomere number adaptations in knee extensor muscles of rats is contraction type dependent. J Appl Physiol 99:1352–1358.
- Camp AL, Brainerd EL. 2014. Role of axial muscles in powering mouth expansion during suction feeding in largemouth bass (*Micropterus salmoides*). J Exp Biol 217:1333–1345.
- Camp AL, Brainerd EL. 2015. Reevaluating musculoskeletal linkages in suction-feeding fishes with X-Ray Reconstruction of Moving Morphology. Integr Comp Biol 55:36–47.
- Camp AL, Roberts TJ, Brainerd EL. 2015. Swimming muscles power suction feeding in largemouth bass. Proc Natl Acad Sci USA 112:8690–8695.
- Camp AL, Astley HC, Horner AM, Roberts TJ, Brainerd EL. 2016. Fluoromicrometry: A method for measuring muscle length dynamics with biplanar videofluoroscopy. J Exp Zool Part A 325: 399–408.
- Cavagna GA, Dusman B, Margaria R. 1968. Positive work done by a previously stretched muscle. J Appl Physiol 24:21–32.
- Cavagna GA, Citterio G. 1974. Effect of stretching on the elastic characteristics and the contractile component of frog striated muscle. J Physiol 239:1–14.
- Cavagna GA, Mantovani M, Willems PA, Musch G. 1997. The resonant step frequency in human running. Eur J Physiol 434:678–684.
- Cavanagh PR, Komi PV. 1979. Electromechanical delay in human skeletal muscle under concentric and eccentric contractions. Eur J Appl Physiol 42:159–163.
- Charles JP, Cappellari O, Spence AJ, Hutchinson JR, Wells DJ. 2016a. Musculoskeletal geometry, muscle architecture and functional specializations of the mouse hindlimb. PLoS One 11:1–22.
- Charles JP, Cappellari O, Spence AJ, Hutchinson JR, Wells DJ. 2016b. Muscle moment arms and sensitivity analysis of a mouse hindlimb musculoskeletal model. J Anat 299:514–535.
- Clark RW, Luschei ES, Hoffman DS. 1978. Recruitment order, contractile characteristics, and firing patterns of motor units in the temporalis muscle of monkeys. Exp Neurol 61:31–52.
- Clarkson PM, Hubal MJ. 2002. Exercise-induced muscle damage in humans. Am J Phys Med Rehabil 81:S52–S69.
- De Brito Fontana H, Herzog W. 2016. Vastus lateralis maximum force-generating potential occurs at optimal fascicle length regardless of activation level. Eur J Appl Physiol 116:1267–1277.

- De Ruiter CJ, Verdijk PW, Werker W, Zuidema MJ, de Haan A. 2014. Stride frequency in relation to oxygen consumption in experienced and novice runners. Eur J Sport Sci 14:251–258.
- Deban SM, O'Reilly JC, Dicke U, van Leeuwen JL. 2007. Extremely high-power tongue projection in plethodontid salamanders. J Exp Biol 210:655–667.
- Delp SL, Anderson FC, Arnold AS, Loan P, Habib A, John CT, Guendelman E, Thelen DG. 2007. OpenSim: Open-source software to create and analyze dynamic simulations of movement. IEEE T Bio-Med Eng 54:1940–1950.
- Dick TJM, Arnold AS, Wakeling JM. 2016. Quantifying Achilles tendon force *in vivo* from ultrasound images. J Biomech 49:3200–3207
- Dick TJM, Biewener AA, Wakeling JM. 2017. Comparison of human gastrocnemius forces predicted by Hill-type muscle models and estimated from ultrasound images. J Exp Biol 220:1643–1653.
- Dickinson E, Stark H, Kupczik K. 2018. Non-destructive determination of muscle architectural variables through the use of diceCT. Anat Rec 301:363–377.
- Dickinson MH, Farley CT, Full RJ, Koehl MAR, Kram R, Lehman S. 2000. How animals move: An integrative view. Science 288: 100–106.
- Edgerton VR, Smith JL, Simpson DR. 1975. Muscle fibre type populations of human leg muscles. Histochem J 7:259–266.
- Edman K, Elzinga G, Noble M. 1978. Enhancement of mechanical performance by stretch during tetanic contractions of vertebrate skeletal muscle fibres. J Physiol 281:139–155.
- Eng CM, Ward SR, Vinyard CJ, Taylor AB. 2009. The morphology of the masticatory apparatus facilitates muscle force production at wide jaw gapes in tree-gouging common marmosets (*Callithrix jacchus*). J Exp Biol 212:4040–4055.
- Erdemir A, McLean S, Herzog W, van den Bogert AJ. 2007. Modelbased estimation of muscle forces exerted during movements. Clin Biomech 22:131–154.
- Felder A, Ward SR, Lieber RL. 2005. Sarcomere length measurement permits high resolution normalization of muscle fiber length in architectural studies. J Exp Biol 208:3275–3279.
- Feng X, Cartwright MS, Walker FO, Bargoil JH, Hu Y, Butler SG. 2015. Ultrasonographic evaluation of geniohyoid muscle and hyoid bone during swallowing in young adults. Laryngoscope 125:1886–1891.
- Finni T, Komi PV, Lukkariniemi J. 1998. Achilles tendon loading during walking: Application of a novel optic fiber technique. Eur J Appl Physiol Occup Physiol 77:289–291.
- Finni T, Komi PV, Lepola V. 2000. In vivo human triceps surae and quadriceps femoris muscle function in a squat jump and counter movement jump. Eur J Appl Physiol 83:416–426.
- Franks HA, Crompton AW, German RZ. 1984. Mechanism of intraoral transport in macaques. Am J Phys Anthropol 65:275–282.
- Gans C, Bock WJ. 1965. The functional significance of muscle architecture A theoretical analysis. Ergebnisse Der Anatomie Und Entwicklungsgeschichte 38:115–142.
- Gans C. 1982. Fiber architecture and muscle function. Exerc Sport Sci Rev 10:(1):160–207.
- Gans C, de Vree F. 1987. Functional bases of fiber length and angulation in muscle. J Morphol 192:63–85.
- Gasser HS, Hill AV. 1924. The dynamics of muscular contraction. Proc R Soc B 96: 398–437.
- German RZ, Saxe SA, Crompton AW, Hiiemae KM. 1989. Food transport through the anterior oral cavity in macaques. Am J Phys Anthropol 80:369–377.
- German RZ, Campbell-Malone R, Crompton AW, Ding P, Holman S, Konow N, Thexton AJ. 2011. The concept of hyoid posture. Dysphagia 26:97–98.
- Gidmark NJ, Konow N, Lopresti E, Brainerd EL. 2013. Bite force is limited by the force-length relationship of skeletal muscle in black carp, *Mylopharyngodon piceus*. Bio Lett 9:20121181.
- Gidmark NJ, Tarrant JC, Brainerd EL. 2014. Convergence in morphology and masticatory function between the pharyngeal jaws of grass carp, *Ctenopharyngodon idella*, and oral jaws of amniote herbivores. J Exp Biol 217:1925–1932.

- Gidmark NJ, Taylor C, Lopresti E, Brainerd EL. 2015. Functional morphology of durophagy in black carp, Mylopharyngodon piceus. J Morphol 276:1422–1432.
- Gignac PM, Kley NJ, Clarke JA, Colbert MW, Morhardt AC, Cerio D, Cost IN, Cox PG, Daza JD, Early CM, etal. 2016. Diffusible iodine-based contrast-enhanced Computed Tomography (diceCT): An emerging tool for rapid, high-resolution, 3-D imaging of metazoan soft tissues. J Anat 228:889–909.
- Gignac PM, Erickson GM. 2017. The biomechanics behind extreme osteophagy in *Tyrannosaurus rex*. Sci Rep 7:2012.
- Gilbert RJ, Napadow JV. 2005. Three-dimensional muscular architecture of the human tongue determined *in vivo* with diffusion tensor magnetic resonance imaging. Dysphagia 20:1–7.
- Gilbert RJ, Magnusson LH, Napadow VJ, Benner T, Wang R, Wedeen VJ. 2006. Mapping complex myoarchitecture in the bovine tongue with diffusion-spectrum magnetic resonance imaging. Biophys J 91:1014–1022.
- Gintof C, Konow N, Ross CF, Sanford CPJ. 2010. Rhythmic chewing oral jaws in teleost fishes: A comparison with amniotes. J Exp Biol 213:1868–1875.
- Goldberg LJ, Derfler B. 1977. Relationship among recruitment order, spike amplitude, and twitch tension of single motor units in human masseter muscle. J Neurophysiol 40:879–890.
- Gonzalez RV, Buchanan TS, Delp SL. 1997. How muscle architecture and moment arms affect wrist flexion-extension moments. J Biomech 30:705–712.
- Gordon AM, Huxley AF, Julian FJ. 1966. The variation in isometric tension with sarcomere length in vertebrate muscle fibres. J Physiol 184:170–192.
- Gregor RJ, Roy RR, Whiting WC, Lovely RG, Hodgson JA, Edgerton VR. 1988. Mechanical output of the cat soleus during treadmill locomotion: *In vivo* versus *in situ* characteristics. J Biomech 21:721–732.
- Hartstone-Rose A, Perry JMG, Morrow CJ. 2012. Bite force estimation and the fiber architecture of felid masticatory muscles. Anat Rec. 295:1336–1351
- Hammond AS, Plavcan JM, Ward CV. 2016. A validated method for modeling anthropoid hip abduction in silico. Am J Phys Anthropol 160:529–548.
- Henneman E, Somjen G, Carpenter DO. 1965. Functional significance of cell size in spinal motoneurons. J Neurophysiol 28:560–580.
- Henry HT, Ellerby DJ, Marsh RL. 2005. Performance of guinea fowl Numida meleagris during jumping requires storage and release of elastic energy. J Exp Biol 208:3293–3302.
- Herring SW, Herring SE. 1974. The superficial masseter and gape in mammals. Am Nat 108:561–576.
- Herzog W, Read LJ. 1993. Lines of action and moment arms of the major force-carrying structures crossing the human knee joint. J Anat 182:213–230.
- Herzog W, Powers K, Johnston K, Duvall M. 2015. A new paradigm for muscle contraction. Front Physiol 6:174.
- Herzog W, Schappacher G, DuVall M, Leonard TR, Herzog JA. 2016. Residual force enhancement following eccentric contractions: A new mechanism involving titin. Physiology 31:300–312.
- Higham TE, Biewener AA, Wakeling JM. 2008. Functional diversification within and between muscle synergists during locomotion. Biol Lett 4:41–44.
- Higham TE, Biewener AA. 2011. Functional and architectural complexity within and between muscles: Regional variation and intermuscular force transmission. Philos Trans R Soc B 366:1477–1487.
- Hiiemae KM, Hayenga SM, Reese A. 1995. Patterns of tongue and jaw movement in a cinefluorographic study of feeding in the macaque. Arch Oral Biol 40:229–246.
- Hiiemae KM, Palmer JB. 1999. Food transport and bolus formation during complete feeding sequences on foods of different initial consistency. Dysphagia 14:31–42.
- Holliday CM, Tsai HP, Skiljan RJ, George ID, Pathan S. 2013. A 3D interactive model and atlas of the jaw musculature of Alligator mississippiensis. PLoS One 8:e62806.

- Holman SD, Konow N, Lukasik SL, German RZ. 2012. Regional variation in geniohyoid muscle strain during suckling in the infant pig. J Exp Zool Part A 317:359–370.
- Holt NC, Azizi E. 2014. What drives activation-dependent shifts in the force-length curve? Biol Lett 10:20140651.
- Holt NC, Roberts TJ, Askew GN. 2014. The energetic benefits of tendon springs in running: Is the reduction of muscle work important? J Exp Biol 217:4365–4371.
- Holt NC, Azizi E. 2016. The effect of activation level on muscle function during locomotion: Are optimal lengths and velocities always used? Proc Biol Sci 283:20152832.
- Hooper SL, Guschlbauer C, Blumel M, Rosenbaum P, Gruhn M, Akay T, Buschges A. 2009. Neural control of unloaded leg posture and of leg swing in stick insect, cockroach, and mouse differs from that in larger animals. J Neurosci 29:4109–4119.
- Hooper SL. 2012. Body size and the neural control of movement. Curr Biol 22:R318–R322.
- Hoy MG, Zajac FE, Gordon ME. 1990. A musculoskeletal model of the human lower extremity: The effect of muscle, tendon, and moment arm on the moment-angle relationship of musculotendon actuators at the hip, knee, and ankle. J Biomech 23:157–169.
- Hunter I, Smith GA. 2007. Preferred and optimal stride frequency, stiffness and economy: changes with fatigue during a 1-h high-intensity run. Eur J Appl 100:653–661.
- Hutchinson JR, Anderson FC, Blemker SS, Delp SL. 2005. Analysis of hindlimb muscle moment arms in *Tyrannosaurus rex* using a three-dimensional musculoskeletal computer model: Implications for stance, gait, and speed. Paleobiology 31:676–701.
- Hutchinson JR, Rankin JW, Rubenson J, Rosenbluth KH, Siston RA, Delp SL. 2015. Musculoskeletal modelling of an ostrich (*Struthio camelus*) pelvic limb: Influence of limb orientation on muscular capacity during locomotion. PeerJ 3:e1001.
- Hylander WL. 1986. In vivo bone strain as an indicator of masticatory bite force in Macaca fascicularis. Arch Oral Biol 31:149–157.
- Hylander WL, Johnson KR, Crompton AW. 1987. Loading patterns and jaw movements during mastication in *Macaca fascicularis*: A bone-strain, electromyographic, and cineradiographic analysis. Am J Phys Anthropol 72:287–314.
- Hylander WL, Johnson KR. 1989. The relationship between masseter force and masseter electromyogram during mastication in the monkey Macaca fascicularis. Arch Oral Biol 34:713–722.
- Hylander WL, Johnson KR. 1993. Modelling relative masseter force from surface electromyograms during mastication in non-human primates. Arch Oral Biol 38:233–240.
- Hylander WL. 2013. Functional links between canine height and jaw gape in catarrhines with special reference to early hominins. Am J Phys Anthropol 150:247–259.
- Iriarte-Diaz J, Riskin DK, Breuer KS, Swartz SM, Evans AR. 2012. Kinematic plasticity during flight in fruit bats: Individual variability in response to loading. PLoS One 7:e366665.
- Iriarte-Diaz J, Terhune CE, Taylor AB, Ross CF. 2017. Functional correlates of the position of the axis of rotation of the mandible during chewing in non-human primates. Zoology (In press). doi: 10.1016/j.zool.2017.08.006
- Inokuchi H, González-Fernández M, Matsuo K, Brodsky MB, Yoda M, Taniguchi H, Okazaki H, Hiraoka T, Palmer JB. 2014. Electromyography of swallowing with fine wire intramuscular electrodes in healthy human: Activation sequence of selected hyoid muscles. Dysphagia 29:713–721.
- Inokuchi H, González-Fernández M, Matsuo K, Brodsky MB, Yoda M, Taniguchi H, Okazaki H, Hiraoka T, Palmer JB. 2016. Electromyography of swallowing with fine wire intramuscular electrodes in healthy human: Amplitude difference of selected hyoid muscles. Dysphagia 31:33–40.
- Jeffery NS, Stephenson RS, Gallagher JA, Jarvis JC, Cox PG. 2011.
  Micro-computed tomography with iodine staining resolves the arrangement of muscle fibres. J Biomech 44:189–192.
- Joumaa V, Rassier DE, Leonard TR, Herzog W. 2008. The origin of passive force enhancement in skeletal muscle. Am J Physiol Cell Physiol 294:C74–C78.

Joumaa V, Herzog W. 2013. Energy cost of force production is reduced after active stretch in skinned muscle fibres. J Biomech 46:1135–1139.

- Kandel ER, Schwartz JH, Jessell TM, Siegelbaum SA, Hudspeth AJ. 2012. Principles of neural science. 5th ed. New York: McGraw-Hill.
- Kargo WJ, Rome LC. 2002. Functional morphology of proximal hindlimb muscle in the frog Rana pipiens. J Exp Biol 205:1987–2004.
- Keefe DF, O'Brien TM, Baier DB, Gatesy SM, Brainerd EL, Laidlaw DH. 2008. Exploratory visualization of animal kinematics using instantaneous helical axes. Comput Graph Forum 27:863– 870.
- Kier WM, Smith KK. 1985. Tongues, tentacles and trunks: The biomechanics of movement in muscular-hydrostats. Zool J Linn Soc 83:307–324
- Kilbourne BM, Hoffman LC. 2013. Scale effects between body size and limb design in quadrupedal mammals. PLoS One 8:e78392.
- Kilbourne BM, Hoffman LC. 2015. Energetic benefits and adaptations in mammalian limbs: scale effects and selective pressures. Evolution 69:1546–1559.
- Knörlein BJ, Baier DB, Gatesy SM, Laurence-Chasen JD, Brainerd EL. 2016. Validation of XMALab software for marker-based XROMM. J Exp Biol 219:3701–3711.
- Koh TJ, Herzog W. 1998. Increasing the moment arm of the tibialis anterior induces structural and functional adaptation: Implications for tendon transfer. J Biomech 31:593–599.
- Komi PV, Belli A, Huttunen V, Bonnefoy R, Geyssant A, Lacour JR. 1996. Optic fibre as a transducer of tendomuscular forces. Eur J Appl Physiol O 72:278–280.
- Konow N, Thexton A, Crompton AW, German RZ. 2010. Regional differences in length change and electromyographic heterogeneity in sternohyoid muscle during infant mammalian swallowing. J Appl Physiol 109:439–448.
- Konow N, Azizi E, Roberts TJ. 2012. Muscle power attenuation by tendon during energy dissipation. Proc Biol Sci 279:1108–1113.
- Konow N, Cheney JA, Roberts TJ, Waldman JR, Swartz SM. 2015. Spring or string: Does tendon elastic action influence wing muscle mechanics in bat flight? Proc Biol Sci 282:1–7.
- Kupczik K, Stark H, Mundry R, Neininger FT, Heidlauf T, Röhrle O. 2015. Reconstruction of muscle fascicle architecture from iodine-enhanced microCT images: A combined texture mapping and streamline approach. J Theor Biol 382:34–43.
- Lauder GL. 1990. Functional morphology and systematics: Studying functional patterns in an historical context. Annu Rev Ecol Syst 21:317–340
- Lauder GL. 1995. On the inference of function from structure. In: Thomason J, editor. Functional morphology in vertebrate paleontology. Cambridge: Cambridge University Press. p 1–18.
- Lauder GV. 1996. The argument from design. In: Rose MR, Lauder GV, editors. Adaptation. San Diego: Academic Press. p 55–91.
- Lautenschlager S. 2015. Estimating cranial musculoskeletal constraints in theropod dinosaurs. R Soc Open Sci 2:150495.
- Lee SSM, Arnold AS, Miara M. d B, Biewener AA, Wakeling JM. 2013. Accuracy of gastrocnemius muscles forces in walking and running goats predicted by one-element and two-element Hill-type models. J Biomech 46:2288–2295.
- Leonard TR, Joumaa V, Herzog W. 2010a. An activatable molecular spring reduces muscle tearing during extreme stretching. J Biomech 43:3063–3066.
- Leonard TR, DuVall M, Herzog W. 2010. Force enhancement following stretch in a single sarcomere. Am J Physiol Cell Physiol 299: C1398–C1401.
- Li Z, Clarke JA, Ketcham RA, Colbert MW, Yan F. 2015. An investigation of the efficacy and mechanism of contrast-enhanced X-ray computed tomography utilizing iodine for large specimens through experimental and simulation approaches. BMC Physiol 15:5
- Li Z, Ketcham RA, Yan F, Maisano JA, Clarke JA. 2016. Comparison and evaluation of the effectiveness of two approaches of diffusible iodine-based contrast-enhanced Computed Tomography (diceCT) for avian cephalic material. J Exp Zool Part B 326:352–362.

- Lieber RL, Fazeli BM, Botte MJ. 1990. Architecture of selected wrist flexor and extensor muscles. J Hand Surg Am 15:244–250.
- Lieber RL, Woodburn RM, Fridén J. 1991. Muscle damage induced by eccentric contractions of 25% strain. J App Physiol 70:2498– 2507.
- Lieber RL, Fridén J. 1993. Muscle damage is not a function of muscle force but active muscle strain. J App Physiol 74:520–526.
- Lieber RL, Ljung BO, Fridén J. 1997. Intraoperative sarcomere length measurements reveal differential design of human wrist extensor muscles. J Exp Biol 200:19–25.
- Lieber RL, Fridén J. 2000. Functional and clinical significance of skeletal muscle architecture. Muscle Nerve 23:1647–1666.
- Lieber RL. 2009. Skeletal muscle structure, function, and plasticity: The physiological basis of rehabilitation. 3rd ed. Baltimore, MD: Lippincott Williams & Wilkins.
- Lieber RL, Ward SR. 2011. Skeletal muscle design to meet functional demands. Philos Trans R Soc Lond B Biol Sci 366:1466–1476.
- Loren GJ, Shoemaker SD, Burkholder TJ, Jacobson MD, Friden J, Lieber RL. 1996. Human wrist motors: biomechanical design and application to tendon transfers. J Biomech 29:331–342.
- Mackenna BR, Türker KS. 1978. Twitch tension in the jaw muscles of the cat at various degrees of mouth opening. Arch Oral Biol 23: 917–920.
- Maganaris CN, Baltzopoulos V, Tsaopoulos D. 2006. Muscle fibre length-to-moment arm ratios in the human lower limb determined *in vivo*. J Biomech 39:1663–1668.
- Marsh RL, Ellerby DJ, Carr JA, Henry HT, Buchanan CI. 2004. Partitioning the energetics of walking and running: Swinging limbs is expensive. Science 303:80–83.
- Matsuo K, Palmer JB. 2010. Kinematic linkage of the tongue, jaw, and hyoid during eating and speech. Arch Oral Biol 55:325–331.
- Mendell L. 2005. The size principle: A rule describing the recruitment of motoneurons. J Neurophysiol 93:3024–3026.
- Menegaz RA, Baier DB, Metzger KA, Herring SW, Brainerd EL. 2015. XROMM analysis of tooth occlusion and temporomandibular joint kinematics during feeding in juvenile miniature pigs. J Exp Biol 218:2573–2584.
- Metscher BD. 2009. MicroCT for comparative morphology: Simple staining methods allow high-contrast 3D imaging of diverse non-mineralized animal tissues. BMC Physiol 9:11.
- Millard M, Uchida T, Seth A, Delp SL. 2013. Flexing computational muscle: Modeling and simulation of musculotendon dynamics. J Biomech Eng 135:21005.
- Milner-Brown HS, Stein RB, Yemm R. 1973. The orderly recruitment of human motor units during voluntary isometric contractions. J Physiol 230:359–370.
- Modica JR, Kram R. 2005. Metabolic energy and muscular activity required for leg swing in running. J App Physiol 98:2126–2131.
- Monroy JA, Powers KL, Pace CM, Uyeno T, Nishikawa KC. 2016. Effects of activation on the elastic properties of intact soleus muscles with a deletion in titin. J Exp Biol doi:10.1242/jeb.139717
- Moo EK, Fortuna R, Sibole SC, Abusara Z, Herzog W. 2016. *In vivo* sarcomere lengths and sarcomere elongations are not uniform across intact muscle. Front Physiol 7:1–9.
- Morhardt AC, Ridgely RC, Witmer LM. 2016. Diffusible iodinebased contrast enhancement of large, post-embryonic, intact vertebrates for CT scanning: Staining, destaining, and long-term storage. In: International Congress of Vertebrate Morphology, June 29–July 3, Bethesda MD.
- Muhl ZF. 1982. Active length-tension relation and the effect of muscle pennation on fiber lengthening. J Morphol 173:285–292.
- Nakamura Y, Iriarte-Diaz J, Arce-McShane F, Orsbon CP, Brown KA, Eastment M, Avivi-Arber L, Sessle BJ, Inoue M, Hatsopoulos NG, Ross CF, Takahashi K. 2017. Sagittal plane kinematics of the jaw and hyolingual apparatus during swallowing in *Macaca mulatta*. Dysphagia 32:663–677.
- Nelson FE, Jayne BC. 2001. The effects of speed on the *in vivo* activity and length of a limb muscle during the locomotion in the iguanian lizard *Dipsosaurus dorsalis*. J Exp Biol 204:3507–3522.
- Nishikawa K, Biewener AA, Aerta P, Ahn AN, Chiel HJ, Daley MA, Daniel TL, Full RJ, Hale ME, Hedric TL, Lappin AK, Nichols TR,

- Quinn RD, Satterlie RA, Szymik B. 2007. Neuromechanics: An integrative approach for understanding motor control. Integr Comp Biol 47:16–54.
- Nishikawa KC, Monroy JA, Uyeno TE, Yeo SH, Pai DK, Lindstedt SL. 2012. Is titin a 'winding filament'? A new twist on muscle contraction. Proc R Soc Lond B Biol Sci 279:981–990.
- Norman RW, Komi PV. 1979. Electromechanical delay in skeletal muscle under normal movement conditions. Acta Physiol Scand 106:241–248.
- O'Connor SM, Cheng EJ, Young KW, Ward SR, Lieber RL. 2016. Sarcomere length distribution quantification in whole muscle frozen sections. J Exp Biol (In press). doi: 10.1242/jeb.132084
- Organ JM, Teaford MF, Taylor AB. 2009. Functional correlates of fiber architecture of the lateral caudal musculature in prehensile and nonprehensile tails of the platyrrhini (Primates) and Procyonidae (Carnivora). Anat Rec 292:827–841.
- Okada T, Aoyagi Y, Inamoto Y, Saitoh E, Kagaya H, Shibata S, Ota K, Ueda K. 2013. Dynamic change in hyoid muscle length associated with trajectory of hyoid bone during swallowing: Analysis using 320-row area detector computed tomography. J Appl Physiol 115:1138–1145.
- Olsen AM. 2016. linkR: 3D lever and linkage mechanism modeling. R package version 1.1.1. https://CRAN.R-project.org/package=linkR
- Olsen AM, Westneat MW. 2016. Linkage mechanisms in the vertebrate skull: Structure and function of three-dimensional, parallel transmission systems. J Morphol 277:1570–1583.
- Pace CM, Mortimer S, Monroy JA, Nishikawa KC. 2017. The effects of skeletal muscle titin mutation on walking in mice. J Comp Physiol A 203:67–76.
- Palmer JB, Rudin NJ, Lara G, Crompton AW. 1992. Coordination of mastication and swallowing. Dysphagia 7:187–200.
- Park D, Lee HH, Lee ST, Oh Y, Lee JC, Nam KW, Ryu JS. 2017. Normal contractile algorithm of swallowing related muscles revealed by needle EMG and its comparison to videofluoroscopic swallowing study and high resolution manometry studies: A preliminary study. J Electromyogr Kinesiol 36:81–89.
- Pappas GP, Asakawa DS, Delp SL, Zajac FE, Drace JE. 2002. Non-uniform shortening in the biceps brachii during elbow flexion. J Appl Physiol 92:2381–2389.
- Pearson WG, Langmore SE, Zumwalt AC. 2011. Evaluating the structural properties of suprahyoid muscles and their potential for moving the hyoid. Dysphagia 26:345–351.
- Pearson WG, Taylor BK, Blair J, Martin-Harris B. 2016. Computational analysis of swallowing mechanics underlying impaired epiglottic inversion. Laryngoscope 126:1854–1858.
- Pennycuick CJ. 1975. On the running of the gnu (Connochaetes taurinus) and other animals. J Exp Biol 63:775–799.
- Perreault EJ, Heckman CJ, Sandercock TG. 2003. Hill muscle model errors during movement are greatest within the physiologically relevant range of motor unit firing rates. J Biomech 36:211–218.
- Perry JMG, Hartstone-Rose A, Wall CE. 2011. The jaw adductors of strepsirrhines in relation to body size, diet, and ingested food size. Anat Rec 294:712–728.
- Pontzer H. 2007. Effective limb length and the scaling of locomotor cost in terrestrial animals. J Exp Biol 210:1752–1761.
- Porro LB, Richards CT. 2017. Digital dissection of the model organism *Xenopus laevis* using contrast-enhanced computed tomography. J Anat. 231:169–191.
- Powell PL, Roy RR, Kanim P, Bello MA, Edgerton VR. 1984. Predictability of skeletal muscle tension from architectural determinations in guinea pig hindlimbs. J App Physiol 57:1715–1721.
- Powers K, Nishikawa KC, Joumaa V, Herzog W. 2016. Decreased force enhancement in skeletal muscle sarcomeres with a deletion in titin. J Exp Biol 219:1311–1316.
- Prilutsky BI, Zatsiorsky VM. 2002. Optimization-based models of muscle coordination. Exerc Sport Sci Rev 30:32–38.
- R Core Team. 2017. R: A language and environment for statistical computing. R Foundation for Statistical Computing, Vienna, Australia. URL http://www.R-project.org/.
- Rabey KN, Green DJ, Taylor AB, Begun DR, Richmond BG, McFarlin SC. 2015. Locomotor activity influences muscle

- architecture and bone growth but not muscle attachment site morphology. J Hum Evol 78:91–102.
- Rack PM, Westbury DR. 1969. The effects of length and stimulus rate on tension in isometric cat soleus muscle. J Physiol 204:443–460.
- Raichlen DA. 2004. Convergence of forelimb and hindlimb Natural Pendular Period in baboons (Papio cynocephalus) and its implication for the evolution of primate quadrupedalism. J Hum Evol 46: 719–738.
- Ramsey RW, Street SF. 1940. The isometric length-tension diagram of isolated skeletal muscle fibers of the frog. J Cell Compar Physl 15:11–34.
- Reed DA, Ross CF. 2010. The influence of food material properties on jaw kinematics in the primate, *Cebus*. Arch Oral Biol 55:946– 962.
- Reyes, M. F., Trifunovic, N., Sharma ,S., Behzadian, K., Kapelan, Z., & Kennedy, M. D. (2017). Mitigation options for future water scarcity: A case study in Santa Cruz Island (Galapagos Archipelago). Water, 9(8), 597. https://doi.org/10.3390/w9080597
- Roberts TJ, Marsh RL, Weyand PG, Taylor CR. 1997. Muscular force in running turkeys: The economy of minimizing work. Science 275: 1113–1115.
- Roberts TJ, Gabaldón AM. 2008. Interpreting muscle function from EMG: Lessons learned from direct measurements of muscle force. Integr Comp Biol 48:312–320.
- Roberts TJ, Abbott EM, Azizi E. 2011. The weak link: Do muscle properties determine locomotor performance in frogs?. Phil Trans R Soc Lond B 366:1488–1495.
- Roberts TJ. 2016. Contribution of elastic tissues to the mechanics and energetics of muscle function during movement. J Exp Biol 219:266–275.
- Ross CF, Lockwood CA, Fleagle JG, Jungers WL. 2002. Adaptation and behavior in the primate fossil record. In: Plavcan JM, Kay RF, Jungers WL van Schaik CP, editors. Reconstructing behavior in the primate fossil record. New York: Kluwer Academic/Plenum Publishers.
- Ross CF, Patel BA, Slice DE, Strait DS, Dechow PC, Richmond BG, Spencer MA. 2005. Modeling masticatory muscle force in finite element analysis: Sensitivity analysis using principal coordinates analysis. Anat Rec 283: 288–299.
- Ross CF, Dharia R, Herring SW, Hylander WL, Liu ZJ, Rafferty KL, Ravosa MJ, Williams SH. 2007. Modulation of mandibular loading and bite force in mammals during mastication. J Exp Biol 210:1046–1063.
- Ross CF, Reed DA, Washington RL, Eckhardt A, Anapol F, Shahnoor N. 2009. Scaling of chew cycle duration in primates. Am J Phys Anthropol 138:30–44.
- Ross CF, Baden AL, Georgi J, Herrel A, Metzger KA, Reed DA, Schaerlaeken V, Wolff MS. 2010. Chewing variation in lepidosaurs and primates. J Exp Biol 213:572–584.
- Ross CF, Iriarte-Diaz J, Nunn CL. 2012. Innovative approaches to the relationship between diet and mandibular morphology in primates. Int J Primatol 33:632–660.
- Ross CF, Iriarte-Diaz J. 2014. What does feeding system morphology tell us about feeding? Evol Anthropol 23:105–120.
- Ross CF, Iriarte-Diaz J, Platts E, Walsh T, Heins L, Gerstner GE, Taylor AB. 2017. Scaling of rotational inertia of primate mandibles. J Hum Evol 106:119–132.
- Roszek B, Baan GC, Huijing PA. 1994. Decrasing stimulation frequenty-dependent length-force characteristics of rat muscel. J App Physiol 77:2115–2124.
- Rupert JE, Rose JA, Organ JM, Butcher MT. 2015. Forelimb muscle architecture and myosin isoform composition in the groundhog (*Marmota monax*). J Exp Biol 218:194–205.
- Russo M, D'Andola M, Portone A, Lacquaniti F, d'Avella A. 2014. Dimensionality of joint torques and muscle patterns for reaching. Front Comput Neurosci 8:24.
- Sawicki GS, Sheppard P, Roberts TJ. 2015. Power amplification in an isolated muscle-tendon unit is load dependent. J Exp Biol 218: 3700–3709.
- Schlager S. 2017. Morpho: Calculations and visualizations related to geometric morphometrics. R package version 2.5.1. https://CRAN.R-project.org/package=Morpho.

- Sellers KC, Middleton KM, Davis JL, Holliday CM. 2017. Ontogeny of bite force in a validated biomechanical model of the American alligator. J Exp Biol 220:2036–2046.
- Seo HG, Oh BM, Han RT. 2016. Swallowing kinematics and factors associated with laryngeal penetration and aspiration in stroke survivors with dysphagia. Dysphagia 31:160–168.
- Slabaugh GG. 1999. Computing Euler angles from a rotation matrix. Internal report. http://thomasbeatty.com/MATH%20-PAGES/ARCHIVES%20-%20NOTES/Applied%20Math/euler%20-angles.pdf, 2016.
- Sokoloff AJ, Yang B, Li H, Burkholder TJ. 2007. Immunohistochemical characterization of slow and fast myosin heavy chain composition of muscle fibres in the styloglossus muscle of the human and macaque (*Macaca rhesus*). Arch Oral Biol 52:533–543.
- Soman A, Hedrick TL, Biewener AA. 2005. Regional patterns of pectoralis fascicle strain in the pigeon *Columba livia* during level flight. J Exp Biol 208:771–786.
- Spector SA, Gardiner PF, Zernicke RF, Roy RR, Edgerton VR. 1980. Muscle architecture and force-velocity characteristics of cat soleus and medial gastrocnemius: Implications for motor control. J Neurophysiol 44:951–960.
- Standring S. 2016. Gray's anatomy: The anatomical basis of clinical practice. 41st ed. Philadelphia PA: Elsevier.
- Steele CM, Van Lieshout P. 2008. The dynamics of lingual-mandibular coordination during liquid swallowing. Dysphagia 23:33–46.
- Stern JT. 1974. Computer modelling of gross muscle dynamics. J Biomech 7:411–428.
- Stevens HC, Snodgrass JM. 1932. The force-velocity curve of striated muscle. Exp Biol Med 30:373–375.
- Takahashi K, Best MD, Huh N, Brown KA, Tobaa AA, Hatsopoulos NG. 2017. Encoding of both reaching and grasping kinematics in dorsal and ventral premotor cortices. J Neurosci 37:1733–1746.
- Taylor AB, Vinyard CJ. 2004. Comparative analysis of masseter fiber architecture in tree-gouging (*Callithrix jacchus*) and nongouging (*Saguinus oedipus*) callitrichids. J Morphol 261:276–285.
- Taylor AB, Jones KE, Kunwar R, Ravosa MJ. 2006. Dietary consistency and plasticity of masseter fiber architecture in postweaning rabbits. Anat Rec 288:1105–1111.
- Taylor AB, Vinyard CJ. 2009. Jaw-muscle fiber architecture in tufted capuchins favors generating relatively large muscle forces without compromising jaw gape. J Hum Evol 57:710–720.
- Taylor AB, Eng CM, Anapol FC, Vinyard CJ. 2009. The functional correlates of jaw muscle fiber architecture in tree-gouging and nongouging callitrichid monkeys. Am J Phys Anthropol 139:353–367.
- Taylor AB, Vinyard CJ. 2013. The relationships among jaw-muscle fiber architecture, jaw morphology, and feeding behavior in extant apes and modern humans. Am J Phys Anthropol 151:120–134.
- Taylor CR. 1985. Force development during sustained locomotion: A determinant of gait, speed and metabolic power. J Exp Biol 115: 253–262.
- Taylor EN, Hoffman MP, Aninwene GE, Gilbert RJ. 2015. Patterns of intersecting fiber arrays revealed in whole muscle with generalized Q-space imaging. Biophys J 108:2740–2749.
- Terhune CE, Iriarte-Diaz J, Taylor AB, Ross CF. 2011. The instantaneous center of rotation of the mandible in nonhuman primates. Integr Comp Biol 51:320–332. doi:10.1093/icb/icr031.
- Terhune CE, Hylander WL, Vinyard CJ, Taylor AB. 2015. Jaw-muscle architecture and mandibular morphology influence relative maximum jaw gapes in the sexually dimorphic *Macaca fascicula-ris*. J Hum Evol 82:145–158.
- Van Hooren B, Zolotarjova J. 2017. The difference between countermovement and squat jump performances: A review of underlying

- mechanics with practical applications. J Strength Cond Res 31: 2011-2020.
- Vickerton P, Jarvis J, Jeffery N. 2013. Concentration-dependent specimen shrinkage in iodine-enhanced microCT. J Anat 223:185– 193.
- Wainwright PC, Alfaro ME, Bolnick DI, Hulsey CD. 2005. Many-toone mapping of form to function: A general principle in organismal design? Integr Comp Biol 45:256–262.
- Wakeling JM, Uehli K, Rozitis AI. 2006. Muscle fibre recruitment can respond to the mechanics of muscle contraction. Interface Focus 3:533–544.
- Wakeling JM, Blake OM, Wong I, Rana M, Lee SSM. 2011. Movement mechanics as a determinate of muscle structure, recruitment and coordination. Philos Trans R Soc Lond B 366:1554–1564
- Wakeling JM, Lee SSM, Arnold AS, Miara MDB, Biewener AA. 2012. A muscle's force depends on the recruitment patterns of its fibers. Ann Biomed Eng 40:1708–1720.
- Wall CE. 1999. A model of temporomandibular joint function in anthropoid primates based on condylar movements during mastication. Am J Phys Anthropol 109:67–88.
- Wang TG, Chang YC, Chen WS, Lin PH, Hsiao TY. 2010. Reduction in hyoid bone forward movement in irradiated nasopharyngeal carcinoma patients with dysphagia. Arch Phys Med Rehabil 91: 926–931.
- Ward SR, Eng CM, Smallwood LH, Lieber RL. 2009a. Are current measurements of lower extremity muscle architecture accurate? Clin Orthop Relat Res 467:1074–1082.
- Ward SR, Takahashi M, Winters TM, Kwan A, Lieber RL. 2009b. A novel muscle biopsy clamp yields accurate *in vivo* sarcomere length values. J Biomech 42:193–196.
- Weijs WA, Korfage JAM, Langenbach GEJ. 1989. The functional significance of the position of the centre of rotation for jaw opening and closing in the rabbit. J Anat 162:133–148.
- Wentzel SE, Konow N, German RZ. 2011. Regional differences in hyoid muscle activity and length dynamics during mammalian head shaking. J Exp Zool Part 315A:111-120.
- Westneat MW. 1990. Feeding mechanics of teleost fishes (Labridae, Perciformes): A test of four-bar linkage models. J Morphol 205: 269–296.
- Westneat MW. 2003. A biomechanical model for analysis of muscle force, power output and lower jaw motion in fishes. J Theor Biol 223:269–281.
- Westneat MW. 2004. Evolution of levers and linkages in the feeding mechanisms of fishes. Integr Comp Biol 44:378–389.
- Williams PE, Goldspink G. 1973. The effect of immobilization on the longitudinal growth of striated muscle fibres. J Anat 116:45–55.
- Winters TM, Takahashi M, Lieber RL, Ward SR. 2011. Whole muscle length-tension relationships are accurately modeled as scaled sarcomeres in rabbit hindlimb muscles. J Biomech 44:109–115.
- Yemm R. 1977. The orderly recruitment of motor units of the masseter and temporal muscles during voluntary isometric contraction in man. J Physiol 265:163–174.
- Young KW, Kuo BP-P, O'Connor SM, Radic S, Lieber RL. 2017. *In vivo* sarcomere length measurement in whole muscles during passive stretch and twitch contractsion. Biophys J 112:805–812.
- Zajac FE. 1989. Muscle and tendon properties, models, scaling, and application to biomechanics and motor control. Crit Rev Biomed Eng 17:359–410.
- Zatsiorsky VM, Prilutsky BI. 2012. Biomechanics of skeletal muscles. Champaign, IL: Human Kinetics.
- Zumwalt A. 2006. The effect of endurance exercise on the morphology of muscle attachment sites. J Exp Biol 209:444–454.